RSC Advances

REVIEW

View Article Online
View Journal | View Issue

Cite this: *RSC Adv.*, 2025, **15**, 29890

Phthalocyanine-nanoparticle conjugates for enhanced cancer photodynamic therapy

Nafeesa Naeem, [a] Amina Sadiq,[b] Hanan A. Ogaly [c] and Ehsan Ullah Mughal *[a]

Photodynamic therapy (PDT) represents a selective and minimally invasive strategy for cancer treatment, relying on light-activated photosensitizers (PSs) to produce ROS that induce tumor cell death. Among various PSs, phthalocyanines have emerged as promising candidates owing to their strong absorption in the near-infrared region, excellent photostability, and high singlet oxygen quantum yield. However, their clinical application remains limited by poor water solubility, tendency to aggregate, and insufficient tumor specificity. To address these challenges, nanoparticle-based delivery systems have been extensively explored to enhance the performance of phthalocyanine (Pc) photosensitizers. This review specifically highlights the integration of metallophthalocyanines (MPcs) with a range of nanoparticles (NPs), including gold, silver, titanium dioxide, magnetic NPs and polymeric carriers. It provides a comprehensive overview of key advancements from 2023 to 2025 in nanoparticle-mediated delivery strategies for phthalocyanine-based PSs in cancer photodynamic therapy. These nanostructures not only improve the solubility and stability of MPcs but also facilitate targeted delivery and enhance photodynamic efficacy through better cellular uptake and controlled release mechanisms. Different classes of nanocarriers and their design strategies for optimizing therapeutic outcomes are critically discussed. Furthermore, the review addresses current challenges such as biological barriers, potential toxicity, and regulatory considerations. Future perspectives on clinical translation are also explored, emphasizing the significant potential of nanoparticle-assisted MPc systems to revolutionize cancer photodynamic therapy.

Received 18th June 2025
Accepted 14th August 2025

DOI: 10.1039/d5ra04347f

rsc.li/rsc-advances

1. Introduction

Cancer remains one of the leading causes of mortality worldwide, prompting the need for innovative treatment strategies.[1] Conventional treatments such as chemotherapy, radiotherapy, and surgical resection often face limitations including non-selectivity, resistance, and severe side effects.[2,3] In this context, photodynamic therapy (PDT) has gained significant attention as a promising non-invasive cancer treatment that uses light-activated PSs to generate ROS, which selectively destroy cancer cells.[4,5] Among the various PSs, phthalocyanines (Pcs) are recognized for their superior photophysical properties, including strong absorption in the near-infrared (NIR) region and high singlet oxygen quantum yield.[6] However, their clinical efficacy is often hindered by issues such as poor solubility, aggregation in biological environments, and limited tumor targeting.[7] The incorporation of nanoparticles (NPs) as carriers for Pc-based PSs provides a promising solution to these challenges by enhancing solubility, stability, and selective accumulation at the tumor site.[8–10] This review explores recent advancements in the development of nanoparticle-assisted Pc systems and their application in cancer PDT.

Initially, the PS, typically a non-toxic molecule in its native state, preferentially accumulates in malignant tissues due to the enhanced permeability and retention (EPR) effect or through active targeting strategies.[11] Upon illumination with light of a specific wavelength, generally matching the PS's absorption maximum, the molecule absorbs photons and transitions from its ground singlet state (S_0) to an excited singlet state (S_1).[12,13] After excitation, the photosensitizer (PS) may undergo inter-system crossing to a longer-lived excited triplet state (T_1), which plays a critical role in initiating photochemical reactions. In the triplet state, the PS can participate in two major types of reactions[14] (Fig. 1). In the type I mechanism, the excited PS directly interacts with nearby biomolecules, such as lipids, proteins, or nucleic acids, through electron or hydrogen atom transfer, resulting in the formation of ROS including superoxide anions, hydroxyl radicals, and hydrogen peroxide.[15] These ROS can induce oxidative damage to essential cellular structures. In the type II mechanism, the triplet-state PS transfers energy directly to ground-state molecular oxygen ($^3O_2$), generating singlet oxygen ($^1O_2$), a highly reactive form of oxygen that can oxidize

[a]Department of Chemistry, University of Gujrat, Gujrat 50700, Pakistan. E-mail: ehsan.ullah@uog.edu.pk
[b]Department of Chemistry, Govt. College Women University, Sialkot 51300, Pakistan
[c]Chemistry Department, College of Science, King Khalid University, Abha 61421, Saudi Arabia

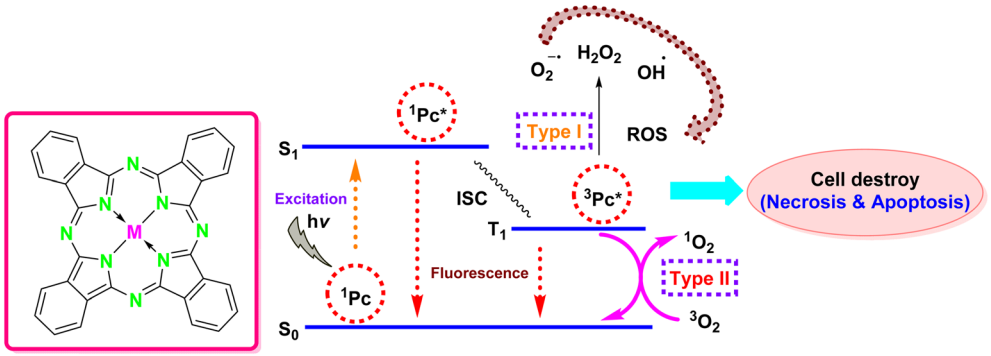

Fig. 1 Schematic representation of the photophysical and photochemical processes involved in PDT, depicted through a modified Jablonski energy level diagram.[14]

cellular membranes, organelles, and DNA, leading to cell death.[16]

The oxidative stress produced by these pathways can trigger various forms of cell death, including apoptosis, necrosis, or autophagy, depending on factors such as the PS concentration, light dose, oxygen availability, and the tumor microenvironment. Moreover, PDT can also damage tumor vasculature and stimulate immune responses against cancer cells, enhancing its overall therapeutic efficacy. Therefore, the precise regulation of light exposure, PS localization, and oxygen presence allows PDT to selectively ablate tumor tissues while minimizing harm to surrounding healthy cells.

2. Phthalocyanines as photosensitizers

Pcs are a class of highly conjugated, synthetic macrocyclic compounds composed of four isoindole units linked by nitrogen atoms to form a planar, aromatic 18-π electron system.[17,18] Structurally, they resemble naturally occurring porphyrins but differ by having nitrogen atoms at the meso positions instead of carbon atoms, typically exhibiting D_{4h} symmetry, which contributes to their remarkable thermal and chemical stability.[19] Pcs possess outstanding electronic and optical properties, making them ideal candidates for PDT.[20] They feature a porphyrin-like core, often coordinated with metal ions such as zinc, copper, or aluminum, which can significantly influence their photophysical behavior. Their strong absorption in the near-infrared (NIR) region (650–800 nm) and high singlet oxygen quantum yield enable deep tissue penetration and potent phototoxic effects under light activated PSs.[21,22] However, despite these advantages, Pcs face significant challenges when utilized *in vivo*, such as poor water solubility and aggregation that reduces their bioavailability and therapeutic efficiency. Additionally, their relatively low tumor specificity further limits their application.[23,24] As a result, enhancing the delivery and targeting of Pcs through nanoparticle systems has become a focal point of research.

Pcs possess a central cavity that can accommodate a wide variety of metal ions, giving rise to metallophthalocyanines (MPcs) (Fig. 2).[25,26] The incorporation of metal ions not only stabilizes the macrocycle but also significantly modifies its electronic, optical, and physicochemical properties.[27,28] Transition metals such as zinc, copper, cobalt, and iron are commonly inserted into the core, tailoring Pcs for diverse applications ranging from catalysis to PDT.[24,29]

The extended π-conjugation throughout the Pc ring system imparts intense absorption in the visible and near-infrared regions, particularly characterized by strong Q-bands and B-bands in the UV-visible spectrum. The position and intensity of these absorption bands are influenced by the nature of the central metal ion and peripheral substituents (Fig. 3).[30] Functionalization at the peripheral or non-peripheral positions of the macrocycle allows further tuning of solubility, aggregation behavior, and photophysical characteristics, critical for biomedical and photonic applications.[31]

3. Advantages of phthalocyanine-based photosensitizers

PCs offer several significant advantages that make them highly attractive for PDT applications (Fig. 4).[32,33] One of the most notable features is their strong absorption in the red to near-infrared (NIR) region of the electromagnetic spectrum, typically between 600 and 800 nm.[34,35] This property allows deeper penetration of light into biological tissues, enabling the treatment of tumors located beneath the surface layers of the skin or internal organs.[36,37]

Another major advantage of Pc derivatives is their high photostability. Unlike many organic dyes, Pcs resist photobleaching under prolonged light exposure, ensuring consistent generation of ROS during the course of therapy.[38] Their extended π-conjugated structure also imparts exceptional chemical and thermal stability, making them suitable for clinical and biomedical applications.[39,40]

Pcs can be readily modified through peripheral or axial substitution, offering versatile strategies to improve their solubility, reduce aggregation, enhance tumor selectivity, and optimize photophysical properties.[41,42] The ability to coordinate various metal ions into the central cavity further expands their functional capabilities, allowing tuning of singlet oxygen quantum yields and photochemical reactivity.[43]

Moreover, Pcs exhibit minimal dark toxicity, meaning they remain largely non-toxic in the absence of light activated PSs.[44] This feature is critical for reducing side effects and enhancing patient safety. Their preferential accumulation in tumor tissues through passive or active targeting mechanisms also contributes to their high therapeutic selectivity.[45]

4. Role of nanoparticles in enhancing photodynamic therapy

Nanotechnology offers a promising approach to overcome the limitations associated with Pc-based PDT.[46] NPs are versatile materials that can be engineered to deliver PSs to the tumor site in a controlled manner.[47] The unique properties of NPs, including their size, surface characteristics, and ability to be functionalized with targeting ligands, make them ideal candidates for improving the pharmacokinetics and biodistribution of PDT agents.[48,49] NPs can improve the solubility of hydrophobic PSs, prevent aggregation, and allow for controlled release of the PS upon exposure to light.[50] Furthermore, NPs can provide enhanced tumor-specific targeting through passive targeting *via* the EPR effect or active targeting using ligands that specifically bind to receptors overexpressed on cancer cells (Fig. 5).[51] These strategies not only enhance the therapeutic efficacy of PDT but also minimize off-target effects, thereby improving patient safety and treatment outcomes. NPs loaded with PS molecules are activated by light exposure, leading to the production of ROS that target and destroy tumor cells.[52]

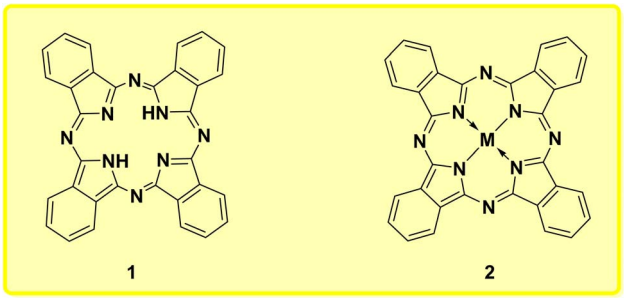

Fig. 2 Structure of phthalocyanine (**1**) and metal phthalocyanine (**2**).

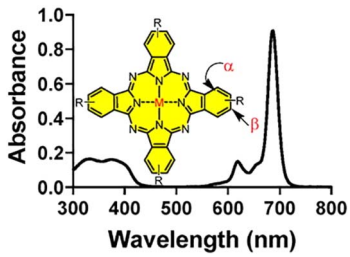

Fig. 3 Absorption spectrum of Pc. Inset: Chemical structure of a Pc molecule, where "*M*" denotes the central metal ion and "*R*" represents the peripheral substituent groups. Reproduced from ref. 30 with permission from Elsevier, copyright © 2021.

5. Metallophthalocyanines (MPcs) with nanoparticles: a synergistic strategy

The combination of MPcs with NPs has emerged as a powerful strategy to overcome the limitations of conventional Pc-based PDT.[53] Metal ions such as zinc, copper, and aluminum can significantly influence the photophysical properties of Pcs, such as their absorption spectra, fluorescence, and singlet oxygen production efficiency. By conjugating MPcs with NPs, several benefits are realized.[54] NPs can enhance the solubility and stability of MPcs, mitigate their tendency to aggregate, and provide a means for targeted delivery to cancer cells.[55] Additionally, NPs can serve as platforms for loading multiple PSs, enabling the simultaneous delivery of drug molecules and photodynamic agents for synergistic therapy.[56] This combination has shown potential in improving the therapeutic outcomes of PDT by increasing the selectivity, stability, and overall efficacy of the treatment.[57,58]

6. Applications of nanoparticles used with metallophthalocyanines

Nyokong *et al.* (2023) examined the *in vitro* anticancer activity of cationic thiazole-substituted Pc, **Pc1** (methylated) and **Pc2** (ethylated) (Fig. 6), in PDT, sonodynamic (SDT), and combined photo-sonodynamic therapy (PSDT). The study assessed the ROS generation, specifically singlet oxygen ($^1O_2$) and hydroxyl radicals ($^{\bullet}OH$), by the free phthalocyanines and their glutathione-stabilized gold (AuGSH) and silver (AgGSH) nanoparticle conjugates in aqueous media under light and

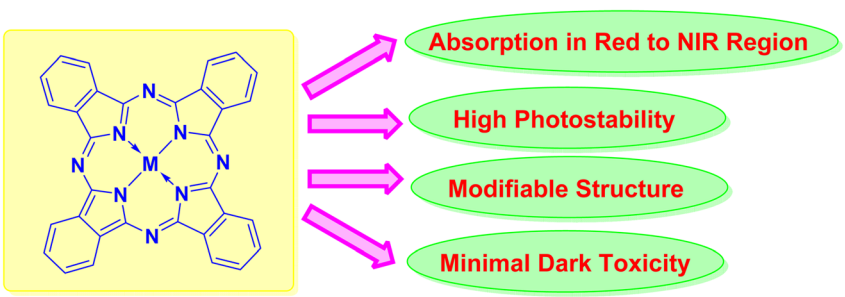

Fig. 4 Advantages of Pc-based photosensitizers.

ultrasound activation (Fig. 7). Both Pc derivatives exhibited ROS production under irradiation, confirming their utility in PDT and SDT. Notably, conjugation with AuGSH and AgGSH NPs enhanced ROS output across all modalities, with PSDT inducing the highest levels of $^1O_2$ and $^{\bullet}OH$. AuGSH-based systems outperformed their AgGSH analogs, likely due to differences in size and surface properties that favored more efficient interactions and energy transfer. Cytotoxicity evaluations in MCF-7 breast cancer cells demonstrated concentration-dependent viability reduction in all treated groups. The most substantial anticancer effect occurred under PSDT, suggesting a synergistic mechanism. While PDT yielded greater $^1O_2$ production, SDT generated a broader spectrum of ROS, contributing to enhanced cytotoxic effects. These findings highlight the potential of metal nanoparticle–phthalocyanine conjugates in augmenting ROS-mediated therapies. For clinical translation, future research should focus on *in vivo* efficacy, biodistribution, and long-term biosafety. The development of ligand-functionalized delivery systems could improve tumor targeting and minimize systemic toxicity. Further mechanistic studies are also needed to elucidate the nanoparticle-facilitated enhancement of ROS generation under dual activation, and integration with imaging modalities may enable the creation of multifunctional theranostic platforms.[59]

Yang *et al.* (2023) successfully encapsulated zinc Pc within boronate-linked polydopamine–Poloxamer 407 NPs, designed to respond to both pH variations and ROS. These nanocarriers demonstrated dual functionality by enabling synergistic photodynamic and photothermal therapeutic effects. The NPs exhibited an average size of 75.02 ± 1.12 nm and remained stable for up to 28 days. Under acidic and ROS-rich conditions, a controlled release reaching 57.29% was achieved over a period of 84 hours. Additionally, the formulation showed a significant cytotoxic effect, inhibiting 73.5% of A549 lung cancer cells at a concentration of 5 μg mL^{-1}. This work presents a promising platform for the delivery of hydrophobic PSs, offering potential for combined photodynamic and photothermal cancer therapies (Fig. 8).[60] Moving forward, further optimization of the nanoparticle surface for active targeting, such as ligand modification for tumor-specific receptors, could significantly improve selective accumulation at tumor sites and minimize off-target effects. Moreover, *in vivo* pharmacokinetics, biodistribution, and long-term toxicity studies are essential to validate the clinical translatability of this platform. While the current system demonstrates promising pH and ROS responsiveness, integrating multi-stimuli sensitivity (*e.g.*, enzyme or temperature-triggered release) may further enhance the precision of therapeutic delivery. Additionally, combining this dual-modal therapy with immunotherapeutic agents or chemotherapeutics could lead to a multifunctional nanoplatform with superior anti-tumor efficacy. Critically, the current work is limited by the lack of comprehensive mechanistic studies exploring the intracellular trafficking and degradation behavior of the NPs, which are vital for understanding therapeutic

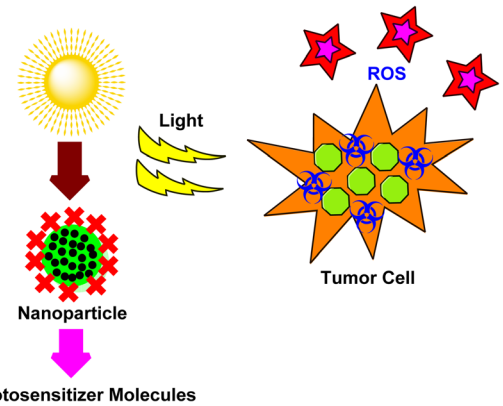

Fig. 5 Schematic illustration of the role of NPs in enhancing PDT.

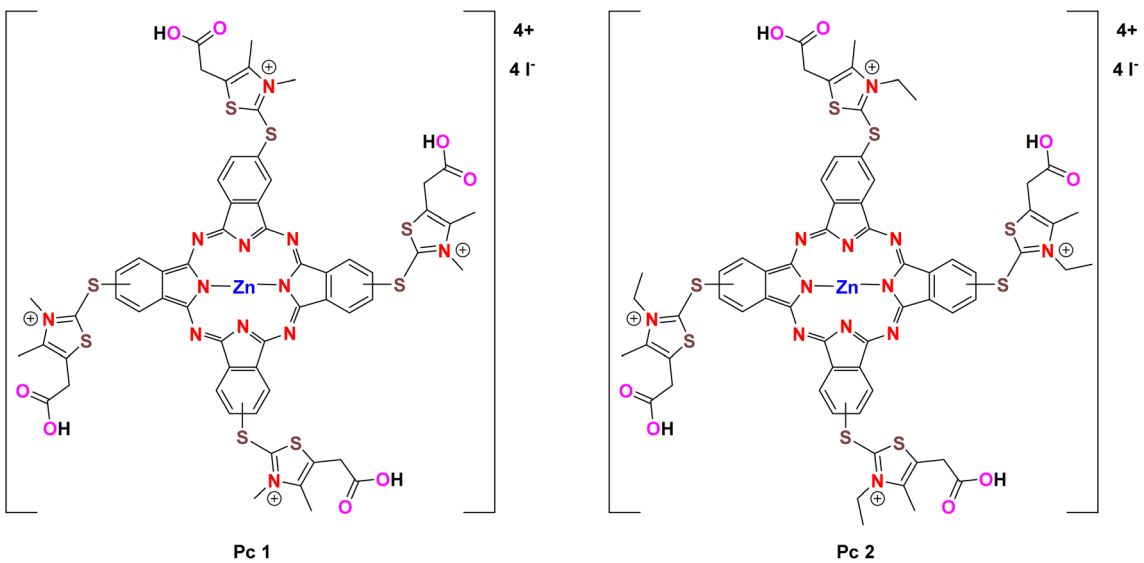

Fig. 6 Chemical structures of Pc1 and Pc2.[59]

outcomes and safety. Addressing these challenges through interdisciplinary approaches involving nanomedicine, molecular biology, and immunotherapy will be key to translating this promising strategy into real-world clinical applications.

Abrahamse *et al.* (2023) investigated the photodynamic therapeutic efficacy of a newly synthesized aluminium(III) chloride phthalocyanine derivative, AlClPcTS41, targeting colorectal cancer (Caco-2) cells (Fig. 9A). The study evaluated both the free PS and its PEGylated copper–gold bimetallic nanoparticle conjugate (AlClPcTS41–PEG-CuAuNPs) for enhanced PDT (Fig. 9B). *In vitro* analyses included cellular uptake, cytotoxicity, and ROS generation upon irradiation at 636 nm. AlClPcTS41 and its nanoparticle formulation demonstrated efficient ROS production following light activated PSs, resulting in significant reductions in Caco-2 cell viability. Importantly, both forms exhibited negligible cytotoxicity in the absence of light, even at concentrations up to 0.58 μM, indicating strong photoselectivity. Lactate dehydrogenase (LDH) release assays confirmed a concentration-dependent cytotoxic response, with the nanoparticle conjugate inducing higher LDH levels than the free PS, suggesting enhanced therapeutic efficacy. The intracellular localization of AlClPcTS41 and its PEG-CuAuNP conjugate was examined *via* fluorescence microscopy. DAPI stained nuclei (blue), while MitoTracker and LysoTracker identified mitochondria and lysosomes (green). AlClPcTS41 showed red fluorescence, which overlapped with green signals to produce yellow, indicating its presence in both organelles. The conjugated form exhibited greater accumulation in

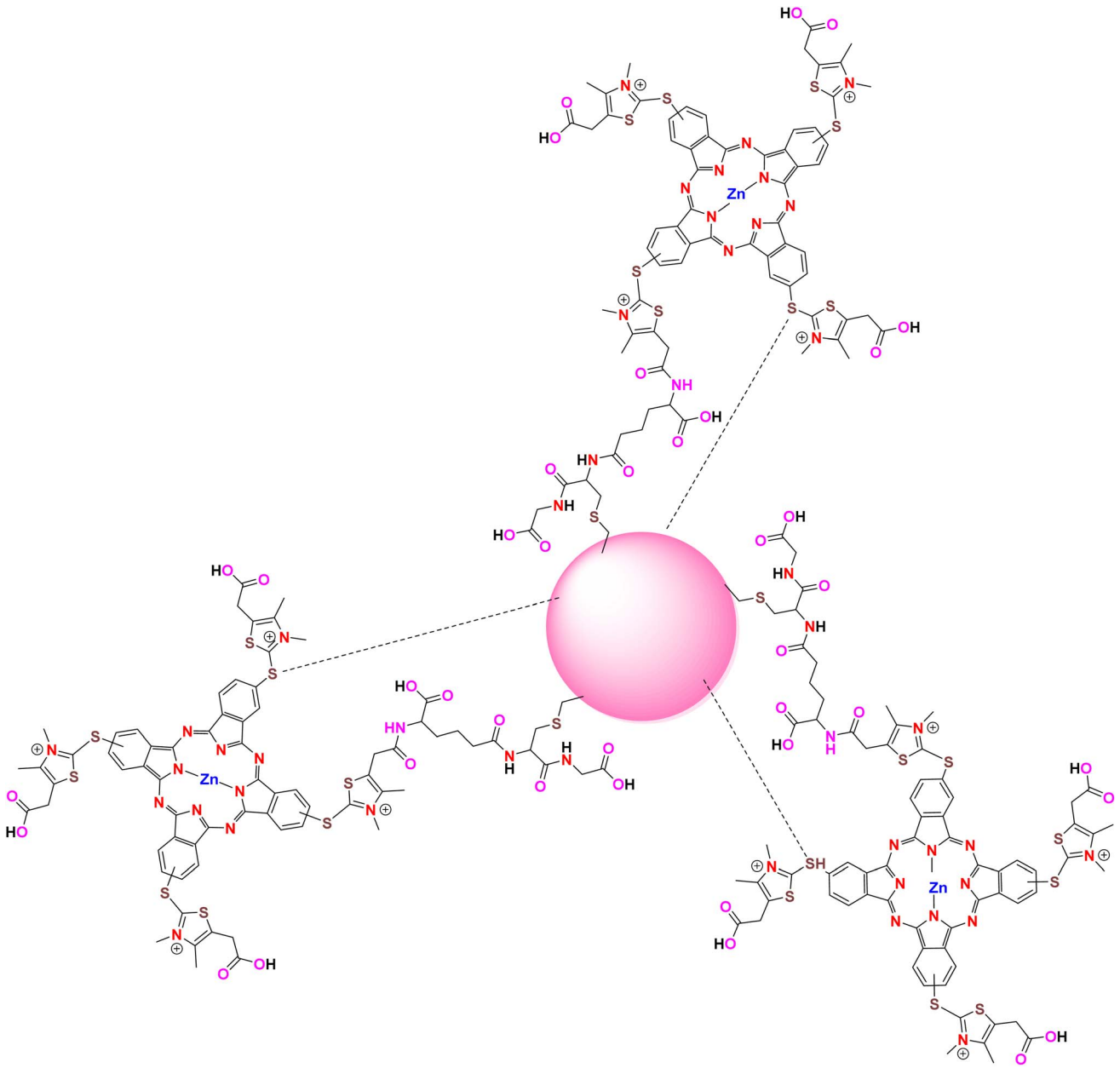

Fig. 7 Conjugation of Pcs to the MPcs.[59]

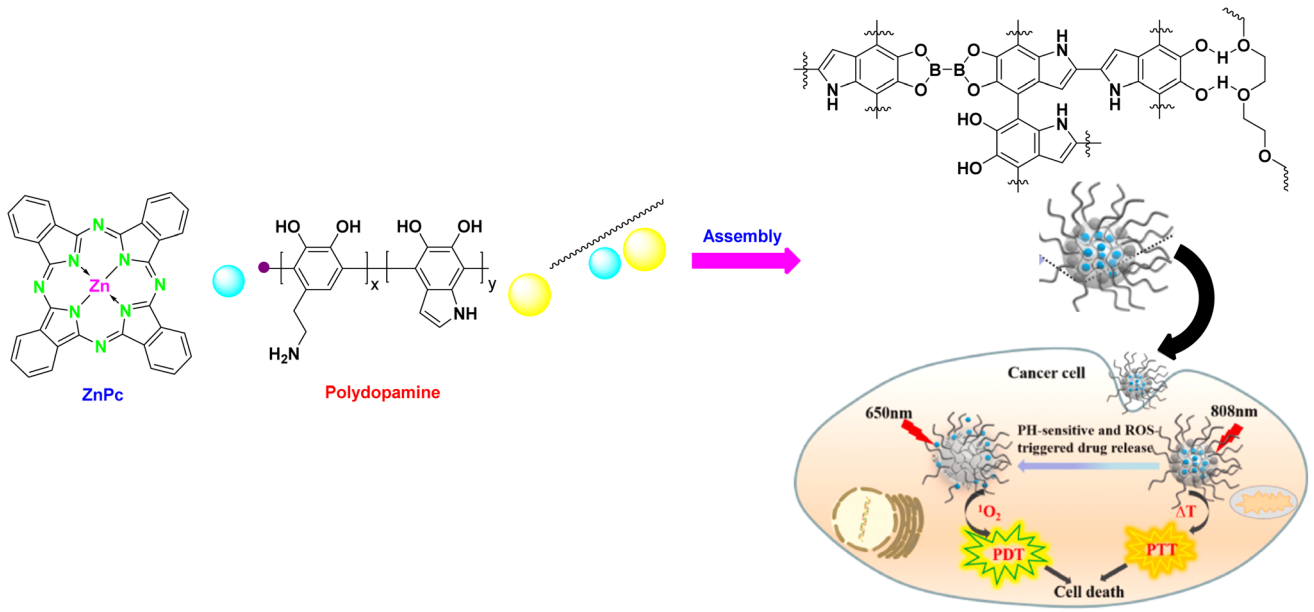

Fig. 8 Chemical structure of ZnPc and schematic representation of the synthesis of ZnPc@PTPNPs, along with the mechanism of their combined photothermal and PDT action against tumors. Reproduced from ref. 60 with permission from Elsevier, copyright © 2023.

mitochondria and lysosomes, suggesting enhanced cellular uptake and targeting compared to the free PS (Fig. 10A–H). ATP-based proliferation assays further validated the superior anticancer activity of the AlClPcTS41–PEG-CuAuNPs under PDT conditions, revealing marked inhibition of cellular proliferation relative to controls. Quantitative ROS measurements confirmed elevated intracellular ROS levels in the PDT-treated conjugate group. These findings underscore the potential of AlClPcTS41, especially in nanoparticle-conjugated form, as an effective PS for PDT of colorectal cancer. The conjugate demonstrated improved cellular uptake, higher ROS-mediated apoptosis, and enhanced phototoxicity. Incorporating tumor-targeting ligands or antibodies may further refine specificity and minimize systemic toxicity. Additionally, optimizing nanoparticle characteristics such as size and surface functionality could enhance bioavailability and therapeutic outcomes.[57]

Abrahamse *et al.* (2023) investigated the photodynamic therapeutic potential of zinc Pc tetrasulfonate ($ZnPcS_4$) conjugated to gold NP (AuNPs) in A375 human melanoma spheroids. Phototoxicity was evaluated under a light fluence of 10 J cm^{-2} using MTT, ATP luminescence, and apoptosis assays. Treatment with free $ZnPcS_4$ (1–20 μM) revealed a concentration-dependent reduction in spheroid viability upon photoactivation, with no cytotoxic effects observed from $ZnPcS_4$ or laser alone. The IC_{50} was determined to be 12.73 μM using dose–response fitting and was employed in subsequent assays. Conjugation of $ZnPcS_4$ to AuNPs significantly enhanced cellular uptake and photodynamic cytotoxicity, primarily *via* apoptosis induction (Fig. 11A and B). These findings highlight the $ZnPcS_4$–AuNP nanoconjugate as a promising candidate for improved PDT in melanoma treatment.[61] The $ZnPcS_4$-AuNP nanoconjugate shows strong potential for melanoma PDT; however, further *in vivo* studies are essential to evaluate pharmacokinetics, biodistribution, and long-term safety. Future efforts should focus on targeted delivery strategies using tumor-specific ligands to enhance selectivity and minimize off-target effects. Optimizing nanoparticle size, shape, and surface chemistry could further improve uptake and efficacy. Mechanistic studies on intracellular localization and ROS-mediated apoptosis are warranted.

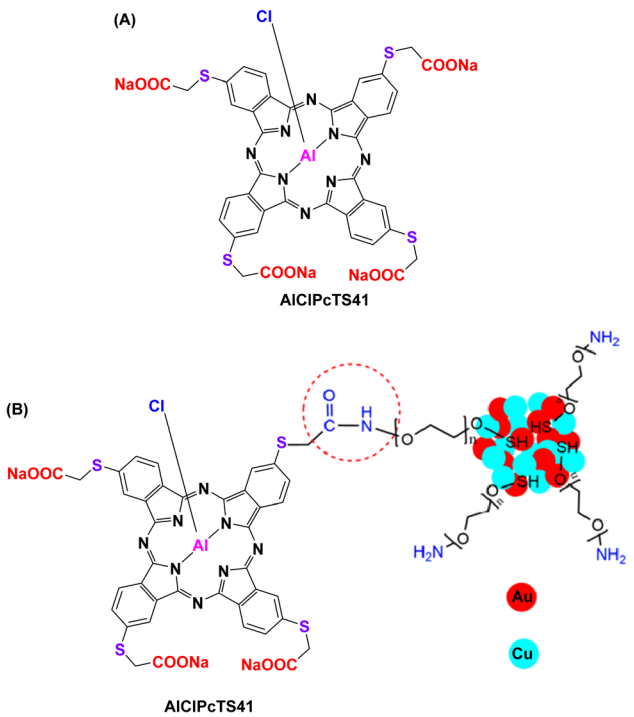

Fig. 9 (A) Chemical structure of AlClPcTS41; (B) chemical structure of AlClPcTS41–PEG-CuAuNP conjugate. Reproduced from ref. 57, under the terms of the CC BY-NC 3.0 license.

Bayır *et al.* (2023) investigated the anticancer potential of silver NP (AgNPs) functionalized with carbazole-substituted phthalonitrile and its Zn, Co, and Mn(Cl) Pc derivatives. These nanoconjugates were synthesized and assessed for cytotoxicity against A549, DLD-1, and Wi38 cell lines using MTT assays under both dark and light conditions. The functionalization improved aqueous solubility and enhanced biological activity. All compounds demonstrated antiproliferative effects, with increased potency upon irradiation. The antiproliferative effects of silver NP (AgNPs) and their nanoconjugates (Fig. 12) were evaluated against two human cancer cell lines (DLD-1 and A549) and one non-cancerous cell line (WI38), using cisplatin as a positive control. Cells were treated with varying concentrations of each compound for 24 hours, both in the presence and absence of white light irradiation. The nanoconjugates exhibited dose-dependent cytotoxicity under both dark and light conditions, as confirmed by MTT assay. Among them, 1-AgNPs showed the strongest activity against DLD-1 cells under light exposure ($IC_{50} = 3.11$ μM), while 3-AgNPs demonstrated notable photo/cytotoxicity against both WI38 ($IC_{50} = 6.05$ μM) and DLD-1 ($IC_{50} = 3.52$ μM) cells. Although 4-AgNPs showed cytotoxic effects at lower concentrations (6.25–25 μM), it displayed a concentration-dependent proliferative response at higher doses, particularly at 50 and 100 μM, suggesting inconsistent biological activity. Particularly, 1-AgNPs induced a proliferative effect on WI38 cells at 100 μM (143.65%). Overall, the nanoconjugates, especially 1-AgNPs and 3-AgNPs, demonstrated superior anticancer potential compared to cisplatin, with statistically significant differences observed in their activity against A549 and WI38 cell lines ($p < 0.05$), regardless of light exposure. However, their anticancer activity against DLD-1 was comparable to that of cisplatin. Nanoconjugates showed selective phototoxicity—exhibiting minimal effects on healthy cells while demonstrating strong activity against cancer cells. These results suggest their potential as alternative anticancer agents to cisplatin, pending further validation.[62]

Zhong *et al.* (2024) developed SiPc–NO self-assembled NPs *via* nanoprecipitation, further modified with RGD for enhanced targeting. The SiPc–NO@RGD NPs (Fig. 13A) significantly inhibited cell migration, reducing wound healing rates by 2.18-fold in 4T1 cells and 4.21-fold in MCF-7 cells compared to non-targeted SiPc–NO@NPs, demonstrating strong anti-migratory potential (Fig. 13B). SiPc–NO@RGD NPs act as targeted carriers for nitric oxide and PSs, enhancing antitumor efficacy and therapeutic safety.[63] However, critical evaluation suggests several areas for further exploration. While the observed reduction in cell migration highlights the anti-metastatic potential, the underlying molecular mechanisms driving this inhibition remain unexplored and warrant detailed investigation. Moreover, the long-term stability, biodistribution, and clearance of these nanocarriers *in vivo* should be thoroughly assessed to validate their clinical applicability. Additionally, comparative studies with conventional therapies and other targeted platforms would help contextualize their therapeutic advantage. Finally, evaluating immunogenic responses and off-target effects is essential to ensure safety and translational viability.

Abrahamse *et al.* (2024) synthesized triphenylphosphine-labeled cationic Pcs and developed a nanoformulation by complexing them with bovine serum albumin and gold NPs (Pc-BSA-Au) (Fig. 14). The photodynamic potential of this complex was compared to free Pc. The Pc-BSA-Au complex exhibited

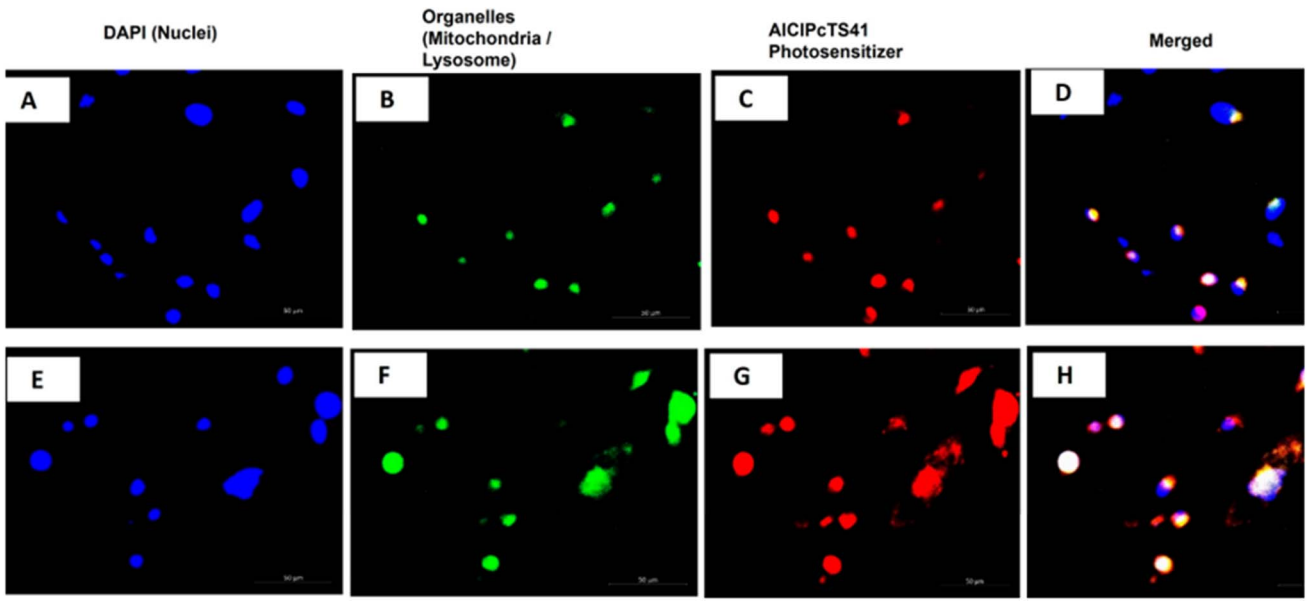

Fig. 10 Fluorescence microscopy analysis of the subcellular distribution of AlClPcTS41–PEG-CuAuNPs in Caco-2 cells. The cells were co-stained with organelle-specific dyes: MitoTracker Green for mitochondria and LysoTracker Green for lysosomes. Panels (A and E) display nuclei stained with DAPI (blue). Panels (B and F) show green fluorescence indicating mitochondria and lysosomes, respectively. Panels (C and G) represent the red fluorescence signal corresponding to AlClPcTS41–PEG-CuAuNPs. Panels (D and H) demonstrate co-localization of the NPs with mitochondria and lysosomes, evidenced by the yellow fluorescence in the merged images (green + red), indicating successful accumulation within both organelles. Reproduced from ref. 57, under the terms of the CC BY-NC 3.0 license.

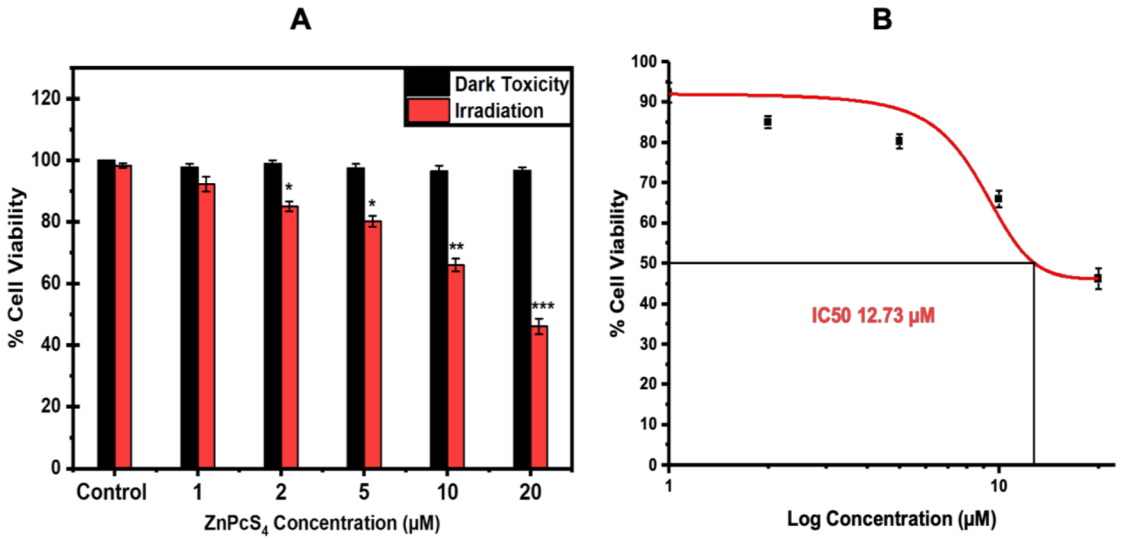

Fig. 11 (A) A375 spheroids treated with increasing concentrations of $ZnPcS_4$ and photoactivated with a 673 nm laser (10 J cm^{-2}). Statistical significance: $p < 0.05$*, $p < 0.01$**, $p < 0.001$*** (B) sigmoidal dose–response curve for IC_{50} determination. Reproduced from ref. 61, under the terms of the CC BY-NC 3.0 license.

a singlet oxygen quantum yield (Φ_Δ) of 0.47 in DMF and demonstrated superior photodynamic efficacy *in vitro* against A375 melanoma cells. Under irradiation, the Pc-BSA-Au treatment reduced cell viability to 23.1%, compared to 48.7% with Pc alone, indicating enhanced cytotoxicity and therapeutic performance.[64]

Zhou *et al.* (2024) developed a novel ZnPc-conjugated periodic mesoporous organosilica (PMO) nanoparticle to overcome the poor solubility and aggregation issues of ZnPc, a promising PS for PDT (Fig. 15A). The PMO NPs maintained their mesoporous structure, exhibited enhanced fluorescence, photostability, and singlet oxygen generation. *In vitro* 4T1 cell assays and *in vivo* tumor-bearing mouse models showed that, upon 675 nm laser irradiation, the ZnPc-PMO NPs effectively produced ROS, significantly suppressing tumor growth. This ZnPc-PMO system offers improved biocompatibility and efficacy, representing a promising platform for advanced PDT applications. Mice receiving intratumoral PMO injection followed by laser irradiation showed significant tumor growth inhibition, whereas PMO or light alone did not affect tumor progression compared to controls. Histological analysis with H&E staining revealed that PDT-treated tumors had disrupted cellular architecture, reduced extracellular matrix, and lower cell density, indicating suppressed tumor proliferation. Mouse body weight remained stable throughout treatment, suggesting minimal systemic toxicity (Fig. 15B–D).[65]

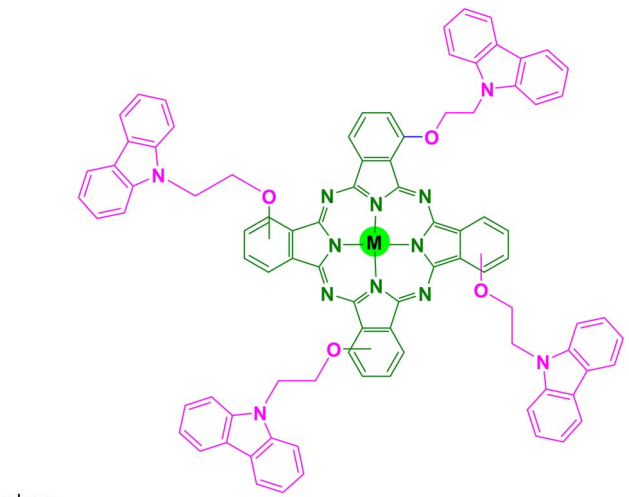

Fig. 12 Chemical structure of MPcs.[62]

Abrahamse *et al.* (2024) explored the therapeutic efficacy of a multifunctional nanobioconjugate composed of AuNPs, the PS ZnPc tetrasulfonic acid ($ZnPcS_4$), and an anti-melanoma inhibitory activity (anti-MIA) monoclonal antibody. This construct was evaluated for its PDT potential against melanoma in both monolayer and three-dimensional spheroid models. The results indicated that the antibody-functionalized nanocarrier significantly enhanced intracellular uptake of the PS in melanoma cells, attributed to the antibody's specific binding affinity to MIA-expressing melanoma cells. The study observed that $ZnPcS_4$ exhibited a significantly faster release rate at pH 5.4 compared to pH 7.4, suggesting that the nanobioconjugate is capable of responding to the acidic conditions of the tumor microenvironment, enabling controlled and site-specific drug release. Upon light activated PSs, the nanoconjugate induced marked cytotoxicity in both cell culture formats. In monolayer assays, treated cells displayed reduced viability and increased apoptotic markers, including nuclear condensation and membrane blebbing. As shown in Fig. 16A, untreated A375 monolayers, as well as cells exposed to laser irradiation alone, free $ZnPcS_4$, or nanoconjugates without irradiation, maintained high levels of viability. However, treatment with 0.85 μM $ZnPcS_4$

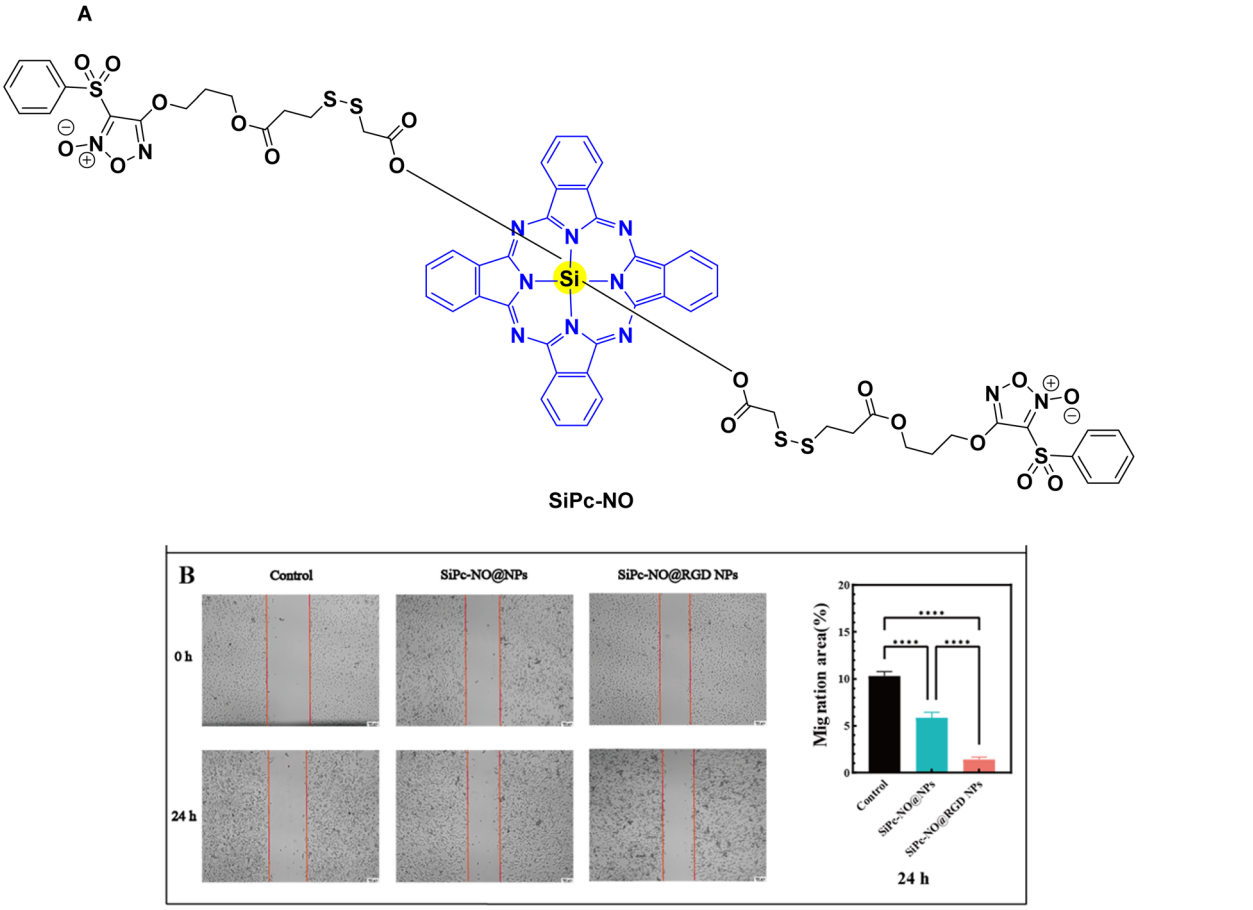

Fig. 13 (A) Chemical structure of SiPc-NO (B) Self-assembled SiPc–NO NPs impair the wound healing capacity of MCF-7 cells. Reproduced from ref. 63, under the terms of the CC BY-NC 3.0 license.

combined with laser exposure led to a marked reduction in cell viability, with a 46.7% decrease in live cells and a significant increase in early and late apoptotic populations to 27.3% and 24.1%, respectively ($p < 0.001$***). PDT using $ZnPcS_4$-AuNPs further enhanced the phototoxic response, decreasing cell viability to 33.7% and raising early and late apoptotic cells to 33.9% and 30.7%, respectively ($p < 0.001$***). The most pronounced cytotoxic effect was observed with NBC-mediated PDT, which resulted in only 15% viable cells, along with substantial increases in early apoptosis (27.6%) and late apoptosis (55.4%) ($p < 0.001$***), indicating a strong PDT-induced apoptotic response. As illustrated in Fig. 16B, PDT mediated by NBC demonstrated the strongest cytotoxic effect, reducing cell viability to 24.3%, while significantly elevating early and late apoptotic populations to 36.6% and 38.7%, respectively ($p < 0.001$***). This elevation in ROS correlated well with observed cell damage, supporting the mechanism of phototoxicity mediated by oxidative stress.[66]

Abrahamse *et al.* (2024) reported the therapeutic potential of a multifunctional nanoplatform composed of zinc phthalocyanine tetrasulfonic acid ($ZnPcS_4$), anti-GCC antibodies, and gold NPs (AuNPs) for PDT in colorectal cancer. The nanoconjugates, characterized by their small spherical morphology, demonstrated potent photocytotoxic effects in both two-dimensional (2D) Caco-2 monolayers and three-dimensional (3D) multicellular tumor spheroids (MCTSs) (Fig. 17A–G). The use of MCTSs, which closely mimic the structural and functional features of avascular tumor tissue, provided a more physiologically relevant model for assessing PDT efficacy. Fig. 18 illustrates that untreated Caco-2 cells exhibited minimal apoptosis, with 94.9% viability. Similarly, over 60% viability was maintained following 24-hour incubation with $ZnPcS_4$, $ZnPcS_4$-AuNPs, or BNC nanoconjugates in the absence of light. However, upon laser activation, all treatment groups showed enhanced apoptotic responses. Particularly, BNC nanoconjugates combined with irradiation induced the highest level of apoptosis, with 71.7% of cells undergoing early apoptosis, 2.3% in late apoptosis, and 0.4% necrosis, indicating strong phototoxic efficacy. Importantly, achieving similar effects in 3D spheroids required higher PS concentrations than in 2D cultures, likely due to the dense cellular architecture and inherent drug resistance of spheroids. Despite this, the nanoconjugates retained significant phototherapeutic potential, supporting their promise for *in vivo* application. These results underscore the value of 3D culture systems in preclinical PDT evaluation. MCTSs bridge the gap between conventional 2D assays and *in vivo* models, offering more accurate insights into therapeutic performance, including drug penetration and resistance. Incorporating additional tumor microenvironment components, such as

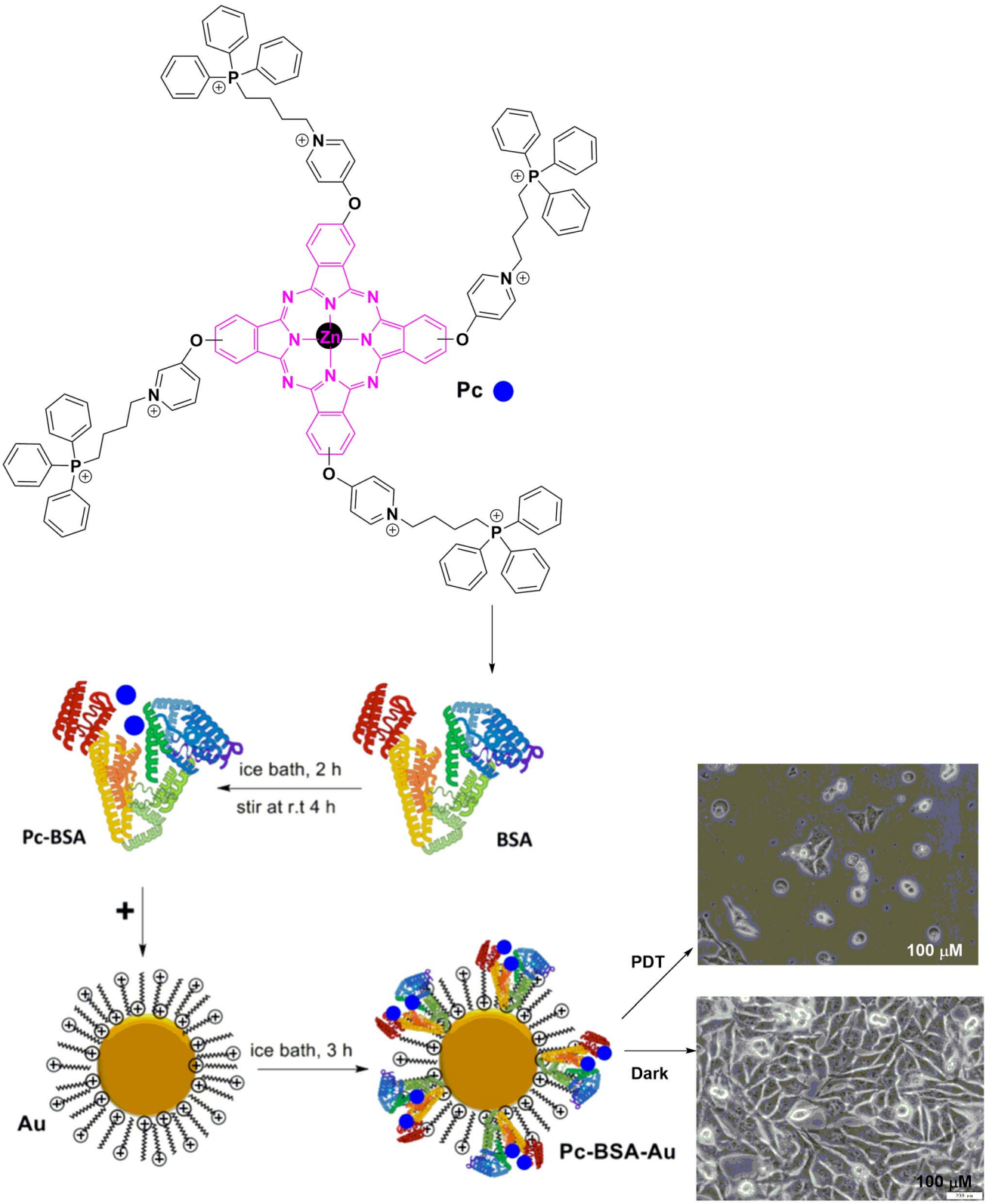

Fig. 14 Synthesis of Pc-BSA-Au nanocomplexes and cellular micrographs captured 24 hours after treatment under dark and PDT conditions with Pc-BSA-Au nanoconjugate. Reproduced from ref. 64 with permission from Elsevier, copyright © 2024.

stromal cells, into these models may further refine targeted PDT approaches for colorectal cancer, ultimately enhancing clinical translation.[67]

Abrahamse *et al.* (2024) employed PDT against both malignant and non-malignant conditions. Aluminium phthalocyanine chloride tetrasulfonate ($AlPcS_4Cl$) has been extensively

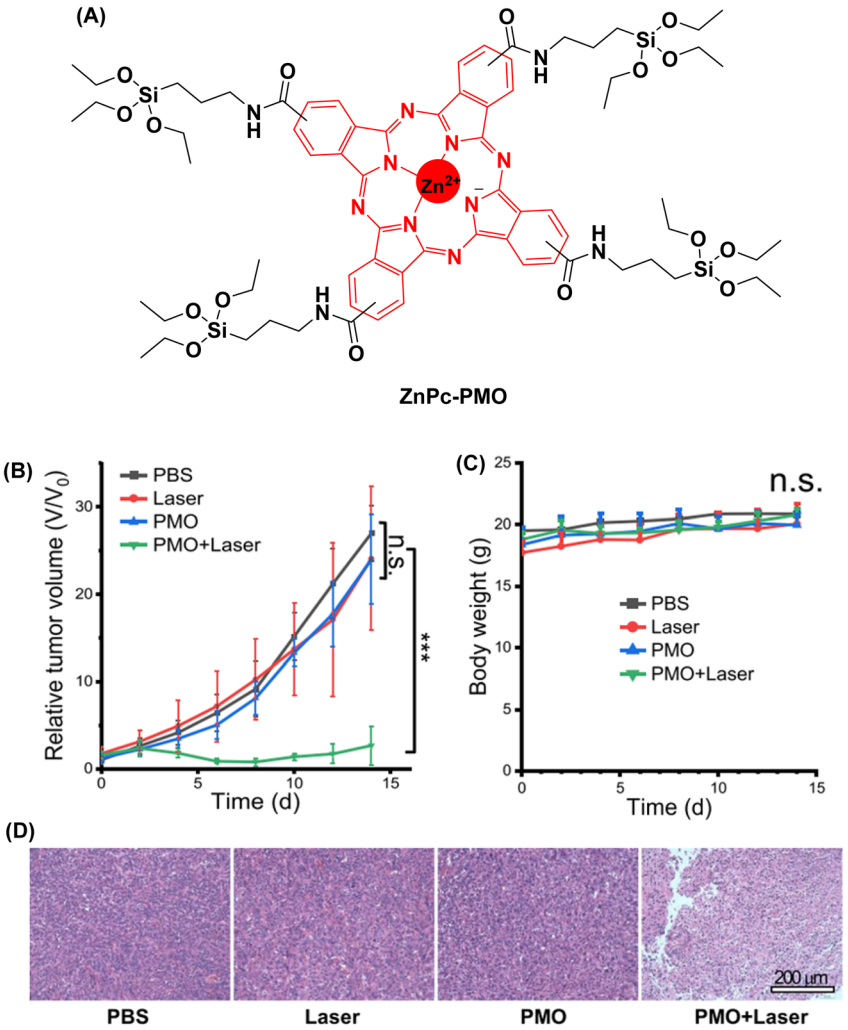

Fig. 15 (A) Chemical structure of ZnPc-PMO. *In vivo* PDT efficacy of PMO: (B) tumor volume progression in treated mice, (C) body weight changes during treatment, and (D) H&E-stained tumor sections post-therapy. Reproduced from ref. 65 with permission from Elsevier, copyright © 2024.

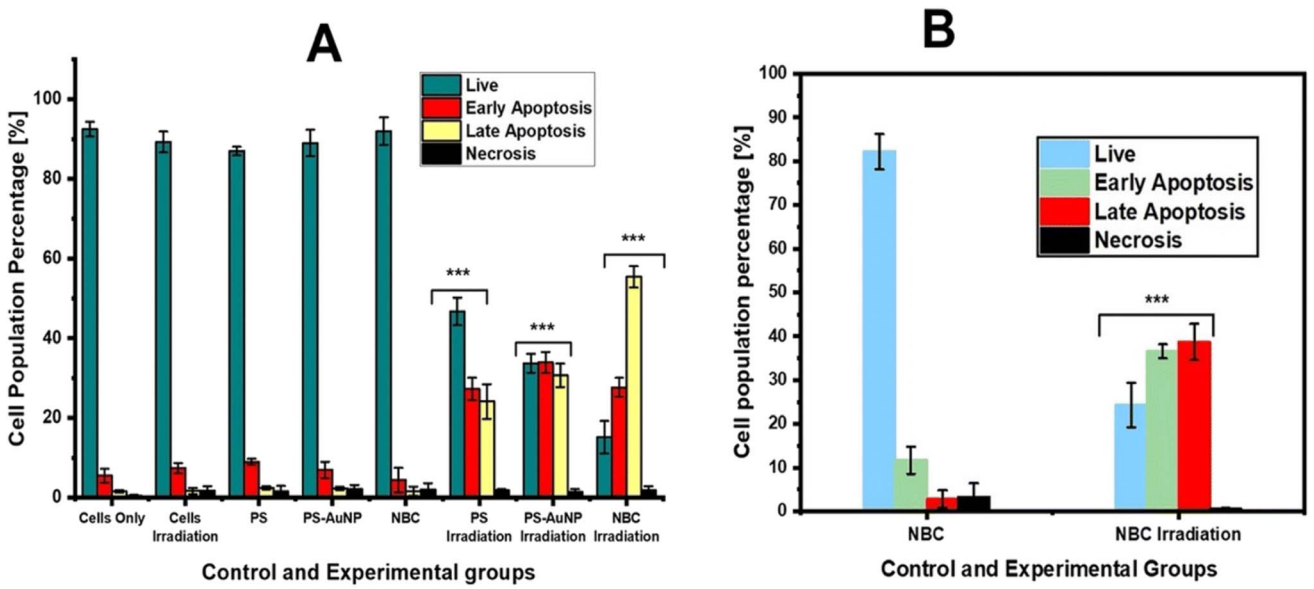

Fig. 16 Modes of cell death in NBC-mediated PDT-treated cells: (A) monolayers and (B) spheroids. Reproduced from ref. 66, under the terms of the CC BY-NC 3.0 license.

studied as a PS in PDT for various cancers, including oesophageal cancer. However, its impact on the DNA damage response and specific pathways of cell death in oesophageal cancer remains to be fully elucidated. Recent findings demonstrated that $AlPcS_4Cl$-mediated PDT significantly decreased cell viability and induced cytotoxic effects, including cell cycle arrest at the G_0/G_1 phase. Moreover, it triggered DNA double-strand breaks (DSBs), which were associated with increased expression of ataxia telangiectasia mutated (ATM), a key sensor in the DNA damage response pathway. The treatment also activated apoptosis, evidenced by elevated ROS levels, a loss of mitochondrial membrane potential ($\Delta\Psi_m$), enhanced cytochrome *c*

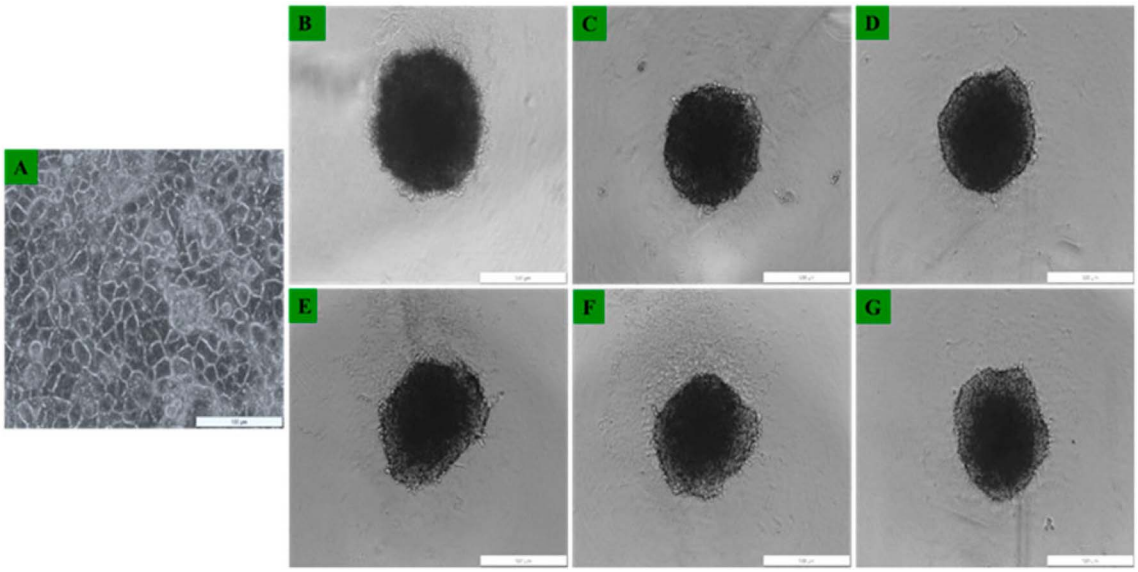

Fig. 17 Representative morphological images of Caco-2 cells: (A) 2D monolayers at 24 h post-seeding; (B–D) 3D multicellular spheroids on day 3; (E–G) spheroids on day 5, captured at 4× magnification. Reproduced from ref. 67, under the terms of the CC BY-NC 3.0 license.

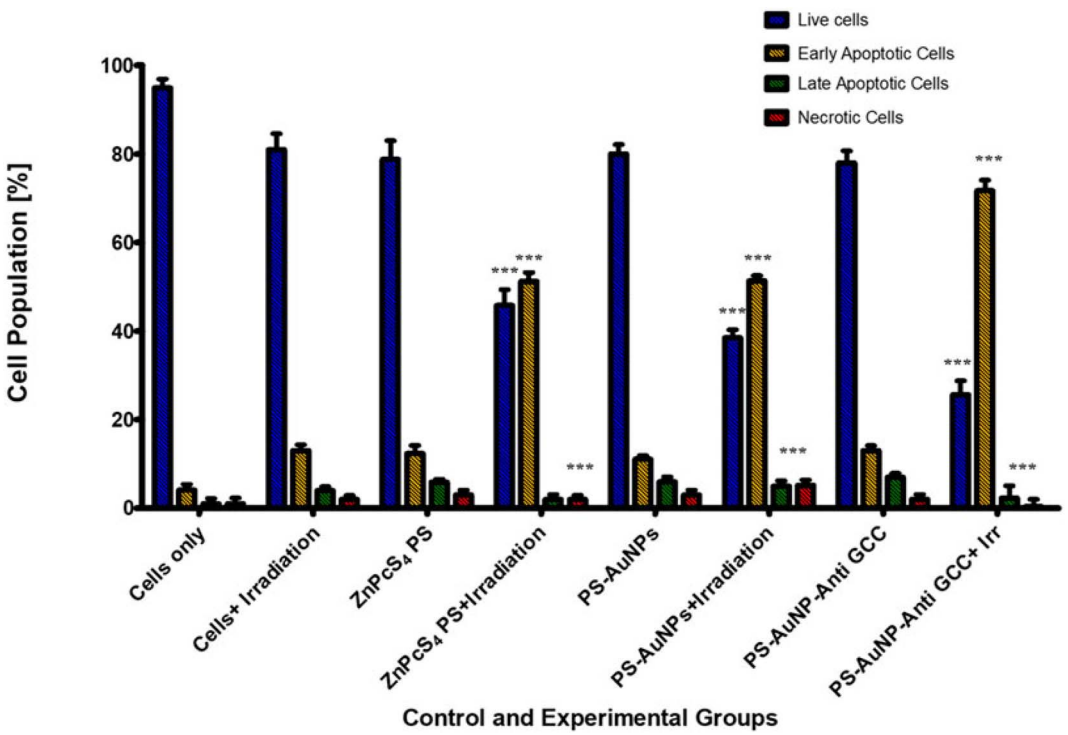

Fig. 18 Flow cytometric analysis of Caco-2 cell apoptosis using Annexin V-FITC/PI staining after treatment with 0.125 μM $ZnPcS_4$, $ZnPcS_4$-AuNPs, or BNC combined with laser irradiation. Controls included untreated cells and those treated without light. Statistical significance was assessed using one-way ANOVA and Dunnett's test (***$p < 0.001$). Reproduced from ref. 67, under the terms of the CC BY-NC 3.0 license.

release, and activation of caspase-3/7 enzymes (Fig. 19A and B). Remarkably, there was no indication of autophagy induction following $AlPcS_4Cl$-based PDT. Fig. 20A–D present histograms of the mean autophagy intensity for control and treated groups. Control cells exhibited an autophagy induction ratio of 1.0, indicating no autophagy induction. Cells treated with laser alone and $AlPcS_4Cl$ without irradiation showed reduced ratios of 0.8 and 0.9, respectively, while $AlPcS_4Cl$-PDT treated cells maintained a ratio of 1.0. Fig. 20E summarizes the percentage mean autophagy intensity from two independent triplicate assays, revealing a significant decrease in autophagy for laser-only and $AlPcS_4Cl$-treated cells ($^*p < 0.05$), whereas no significant change was observed in the $AlPcS_4Cl$-PDT group. Overall, the autophagy induction ratios shown in Fig. 20F indicate no significant autophagy induction across all groups. These results collectively suggest that apoptosis is the predominant mode of

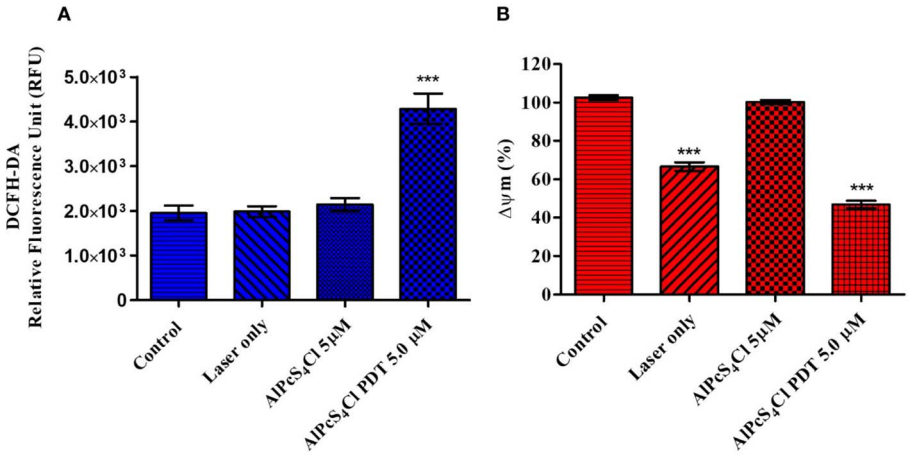

Fig. 19 (A) ROS generation in HKESC-1 cells after AlPcS4Cl-PDT treatment, showing significant increase ($^{***}p < 0.001$). (B) Mitochondrial membrane potential ($\Delta\psi_m$) assessed by rhodamine-123 assay, with significant disruption in irradiated control and $AlPcS_4Cl$-PDT cells ($^{***}p < 0.001$); no change in dark controls. Data represent mean ± SEM from two independent experiments, each in triplicate. Reproduced from ref. 68, under the terms of the CC BY-NC 3.0 license.

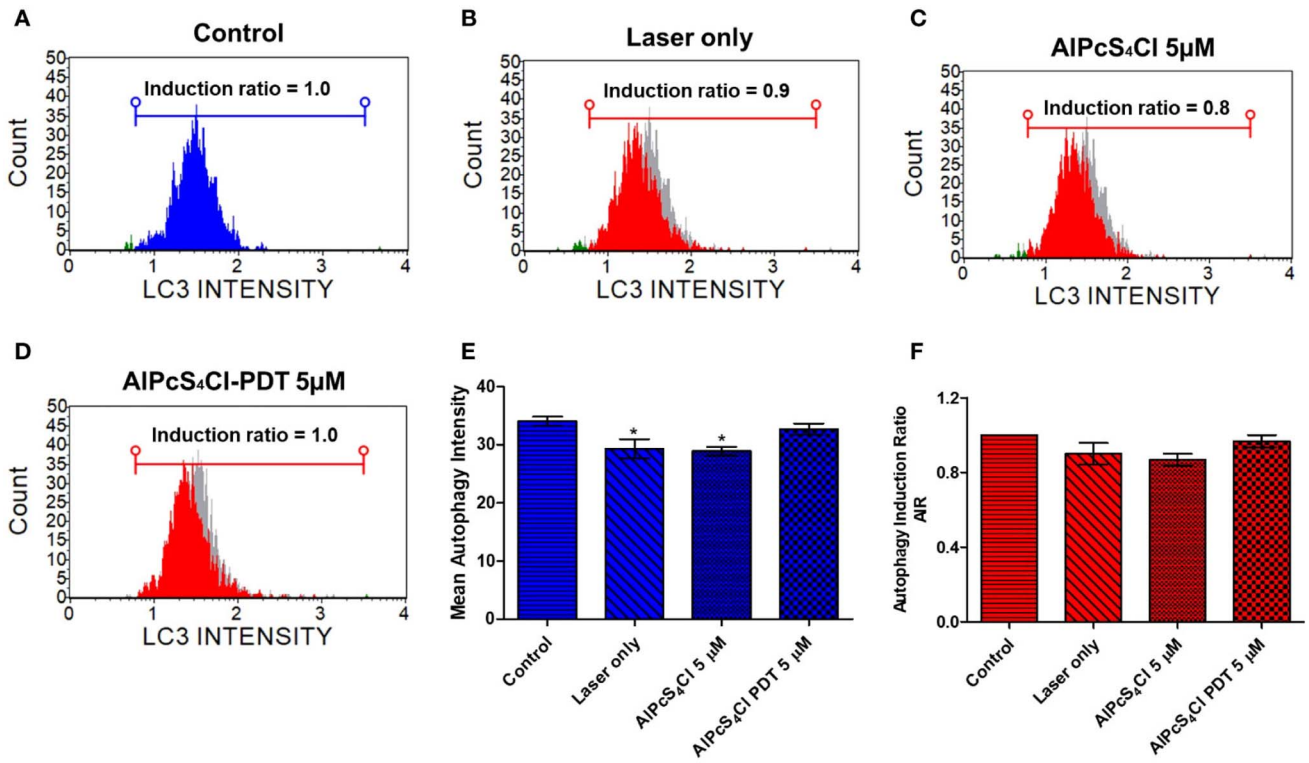

Fig. 20 Assessment of autophagic cell death in esophageal cancer cells (A–F). Reproduced from ref. 68, under the terms of the CC BY-NC 3.0 license.

cell death induced by $AlPcS_4Cl$-mediated PDT in oesophageal cancer cells.[68]

Wang *et al.* (2024) developed a novel series of matrine-based proteolysis-targeting chimeras (PROTACs), named LST-1 LST-2, LST-3 and LST-4, each differing by linker chain length, to overcome the inherent therapeutic limitations of matrine (Fig. 21A and B). Among them, LST-4 exhibited the most potent anti-tumor activity, with effective degradation of phosphorylated Erk (p-Erk) and Akt (p-Akt) proteins. Especially, LST-4 demonstrated the ability to self-assemble into NPs (LST-4 NPs), which enhanced tumor suppression and promoted glutathione (GSH) depletion, with preferential lysosomal accumulation facilitated by the EPR effect. To augment therapeutic outcomes, a dual-functional nanoplatform (LST-4@ZnPc) was constructed by co-loading LST-4 with the PS zinc phthalocyanine (ZnPc). This system enables pH-responsive release of ZnPc within the acidic tumor microenvironment, integrating chemotherapy and PDT. LST-4 NPs contribute chemotherapeutic efficacy and GSH depletion, while ZnPc-mediated PDT increases ROS generation. The synergistic ROS accumulation amplifies cytotoxicity and enhances tumor eradication (Fig. 22A–I). The cytotoxic potential of the synthesized PROTACs was evaluated using the CCK-8 assay in HepG2 (hepatocellular carcinoma) and L02 (normal hepatic) cell lines. All four derivatives exhibited dose-dependent inhibition of HepG2 viability, with LST-4 showing the highest potency (IC_{50} = 106.0 μM), representing a 65.59% improvement over LST-1 (IC_{50} = 162.1 μM). In contrast, all compounds displayed minimal toxicity towards L02 cells (0–400 μM), confirming favorable biosafety (Fig. 23A–F). Based on these findings, LST-4 was selected for further study. The LST-4@ZnPc nanoplatform integrates multiple therapeutic functions—targeted protein degradation, GSH depletion, and PDT—offering a promising strategy for enhanced cancer therapy. This work exemplifies the potential of

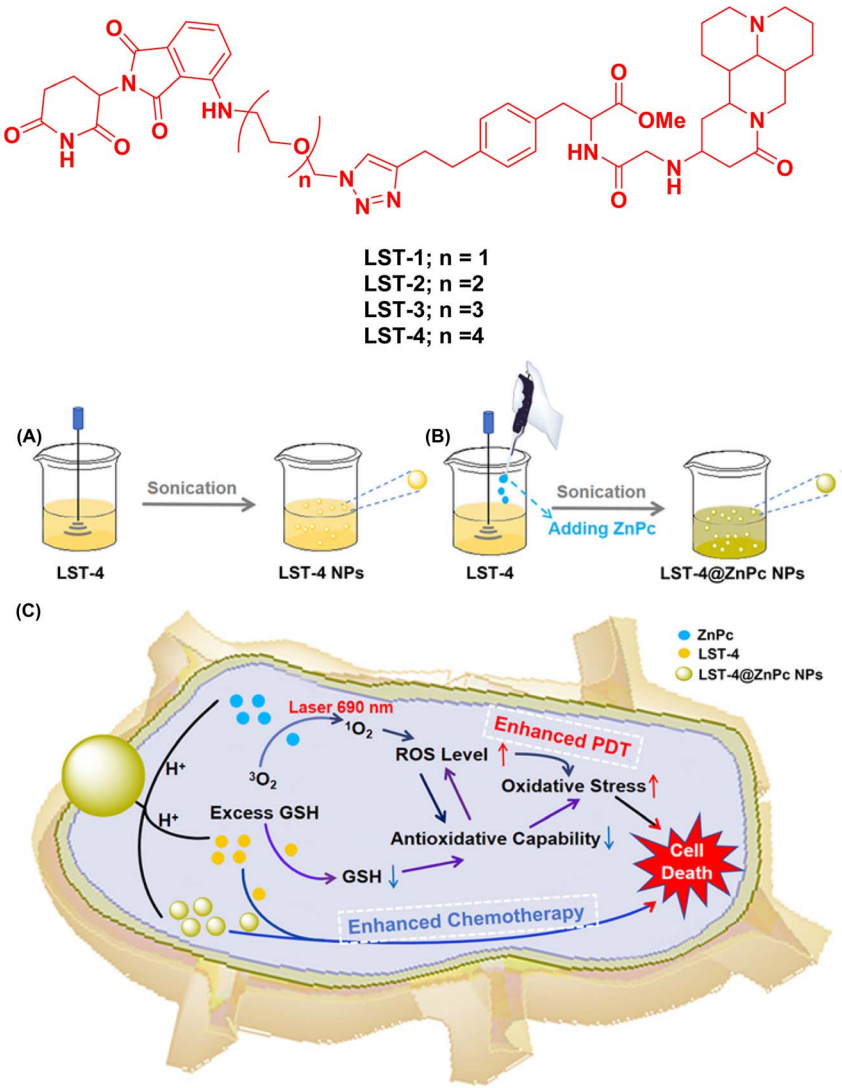

Fig. 21 Chemical structure of LST-1, LS-2, LST-3 and LST-4. Schematic illustration of (A and B) the structure and (C) the therapeutic function of LST-4@ZnPc NPs, highlighting their tumor microenvironment (TME)-responsive, combined chemo-photodynamic strategy for selective and enhanced cancer cell eradication. Reproduced from ref. 69, under the terms of the CC BY-NC 3.0 license.

PROTAC technology and traditional Chinese medicine derivatives in the development of multifunctional, nanostructured cancer therapeutics.[69]

Tsourkas *et al.* (2024) encapsulated approximately 40 structurally distinct naphthalocyanine (NC) and PC dyes into polymeric micelles composed of polyethylene glycol–polycaprolactone (PEG-PCL) using an oil-in-water emulsion method. These dye-loaded micelles were screened to identify the most effective formulations for both PTT and photoacoustic (PA) imaging through comprehensive *in vitro* and *in vivo* evaluations. Pc and NC dyes were encapsulated into PEG–PCL micelles *via* an oil-in-water emulsion method. The resulting micelles showed uniform sizes (35–110 nm), stable zeta potentials (mostly negative), and consistent physicochemical properties across batches. TEM confirmed successful dye loading, and absorbance spectra ranged from 400–900 nm. Representative images and spectral data are shown in Fig. 24A–C. Among the tested candidates, micelles loaded with CuNC(Octa) emerged as the most promising, exhibiting a strong photoacoustic response with peak absorbance around 870 nm, excellent photothermal conversion efficiency, and distinguished photostability. Compared to conventional nanomaterials such as gold nanorods and nanoshells, CuNC(Octa)-loaded micelles demonstrated comparable or superior heat generation and over a tenfold enhancement in PA signal intensity. These micelles also displayed high stability under physiological conditions and could be reliably produced on a scalable basis. To assess the theranostic potential of CuNC(Octa)-loaded micelles, their therapeutic efficacy was investigated in 4T1 tumor-bearing mice across three different dosage levels (Fig. 24D). Leveraging the EPR effect, CuNC(Octa)-loaded micelles preferentially accumulated in tumor tissue, where they were readily visualized using PA imaging. In a syngeneic murine model of triple-negative breast cancer,

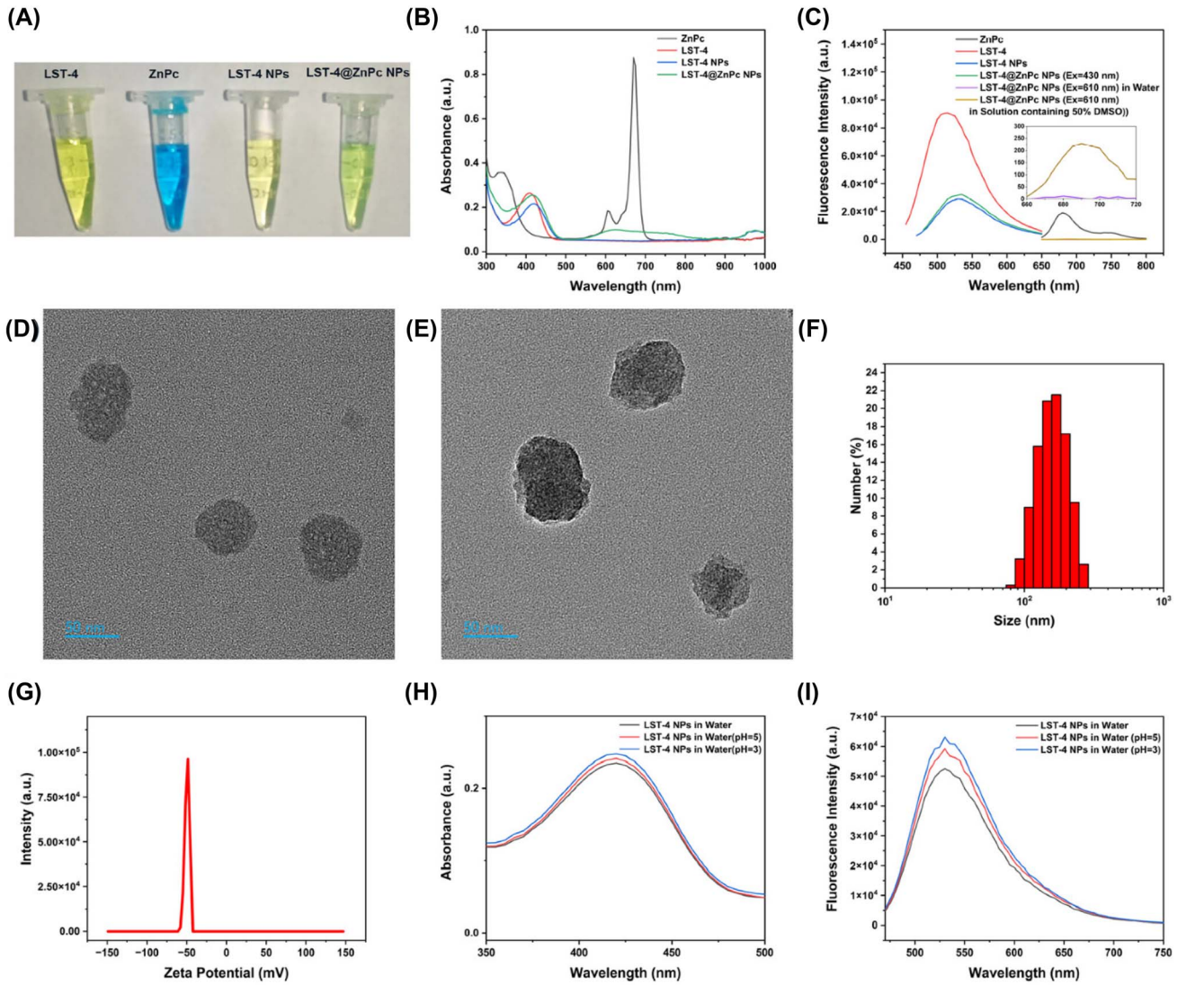

Fig. 22 (A) Images of ZnPc, LST-4, LST-4 NPs, and LST-4@ZnPc NPs. (B) UV-vis spectra and (C) fluorescence intensities of all formulations at 20 μg mL. (D and E) TEM images of LST-4 NPs and LST-4@ZnPc NPs. (F) Size distribution and (G) zeta potential of LST-4@ZnPc NPs. (H and I) pH-dependent UV-vis and fluorescence response of LST-4 NPs. Reproduced from ref. 69, under the terms of the CC BY-NC 3.0 license.

treatment with CuNC(Octa)-loaded micelles combined with PTT resulted in effective heat-mediated ablation and complete tumor eradication. Furthermore, the integration of PA imaging with conventional ultrasound offers real-time insights into tumor structure and micelle biodistribution. These findings position CuNC(Octa)-loaded micelles as a potent theranostic platform for both tumor imaging and PTT, with significant potential for the treatment of aggressive cancers.[70]

Báo *et al.* (2024) reported that PDT holds potential in cancer treatment by inducing immunogenic cell death (ICD), a process marked by the regulated exposure of damage-associated molecular patterns (DAMPs). These DAMPs serve to activate dendritic cells (DCs), thereby modulating immune responses within the tumor microenvironment. Despite its therapeutic potential, PDT remains limited by the poor aqueous stability and low bioavailability of many PSs. To address these challenges, the researchers developed a novel photosensitizing system, SLN-AlPc, designed to enhance the efficacy of PDT. *In vitro* studies using murine B16–F10 melanoma cells demonstrated that upon light activated PSs, the SLN-AlPc nanocarrier significantly increased the generation of ROS. This oxidative stress was associated with the induction of ICD, evidenced by the exposure of DAMPs and the formation of autophagosomes. Furthermore, DCs co-cultured with PDT-treated B16–F10 cells displayed morphological changes indicative of activation, along with elevated expression of major histocompatibility complex class II (MHC II), CD86, and CD80. These cells also secreted higher levels of proinflammatory cytokines such as interleukin-12 (IL-12) and interferon-gamma (IFN-γ), pointing to an enhanced anti-tumor immune response (Fig. 25A–C). As shown in Fig. 26A, the presence of autophagosomes was evident in both the PDT and methotrexate (MTX) treatment groups. Immunofluorescence images (Fig. 26B) revealed that cells subjected to PDT exhibited cytoplasmic accumulation of calreticulin, followed by its translocation and subsequent exposure on the cell surface. In contrast, MTX-treated cells showed a marked localization of calreticulin on the plasma membrane along with the appearance of vesicles containing this protein. These vesicles may play a role in intercellular communication within the tumor microenvironment, potentially contributing to immunogenic signaling. Collectively, these findings suggest that the SLN-AlPc PS system can potentiate PDT outcomes by effectively inducing ICD and activating DCs, representing a promising strategy for improving immune-mediated cancer therapies.[71]

Peng *et al.* (2025) developed a novel multifunctional nanoparticle, designated TPA-BPAF-SiPc@AuNR@SiO_2, synthesized by encapsulating NIR fluorinated triphenylamine-substituted silicon Pcs (TPA-BPAF-SiPc) within mesoporous silica-coated gold nanorods (AuNR@SiO_2). This system acts as a dual-functional two-photon probe, capable of facilitating photoinduced lysosomal escape and mitochondrial targeting (Fig. 27). Remarkably, the TPA-BPAF-SiPc component displays strong aggregation-induced emission (AIE) two-photon fluorescence when confined within the AuNR@SiO_2 matrix—an enhancement not observed with polymer-based nanocarriers such as DSPE-PEG2000 or in THF/water environments. Upon light activated PSs, the nanoparticle escapes from lysosomes and selectively localizes to mitochondria, a process that can be tracked in real-time *via* its two-photon AIE fluorescence. In addition, the system demonstrates efficient ROS generation and

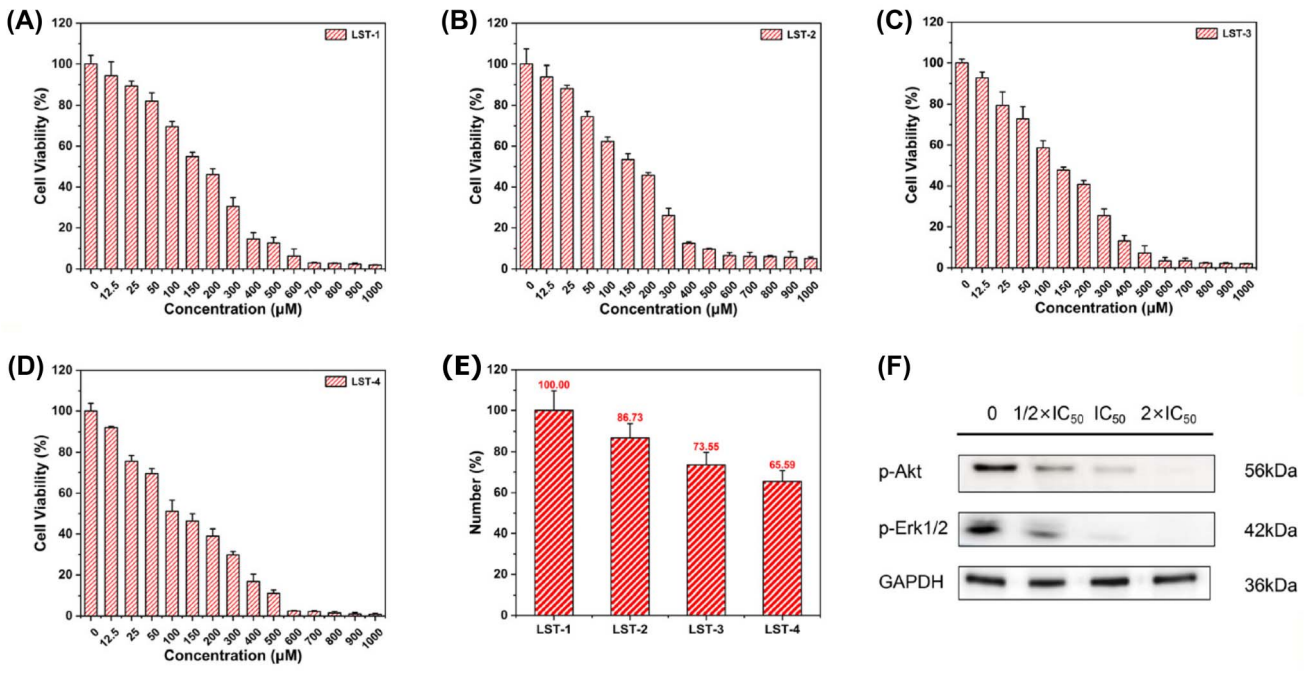

Fig. 23 Viability of HepG2 cells following treatment with increasing concentrations of (A) LST-1, (B) LST-2, (C) LST-3, and (D) LST-4 ($n = 4$). (E) Comparison of IC_{50} values for LST derivatives in HepG2 cells ($n = 3$). (F) Expression levels of p-Akt and p-Erk in HepG2 cells after treatment with 0, 1/2 × IC_{50}, IC_{50}, and 2 × IC_{50} concentrations. Reproduced from ref. 69, under the terms of the CC BY-NC 3.0 license.

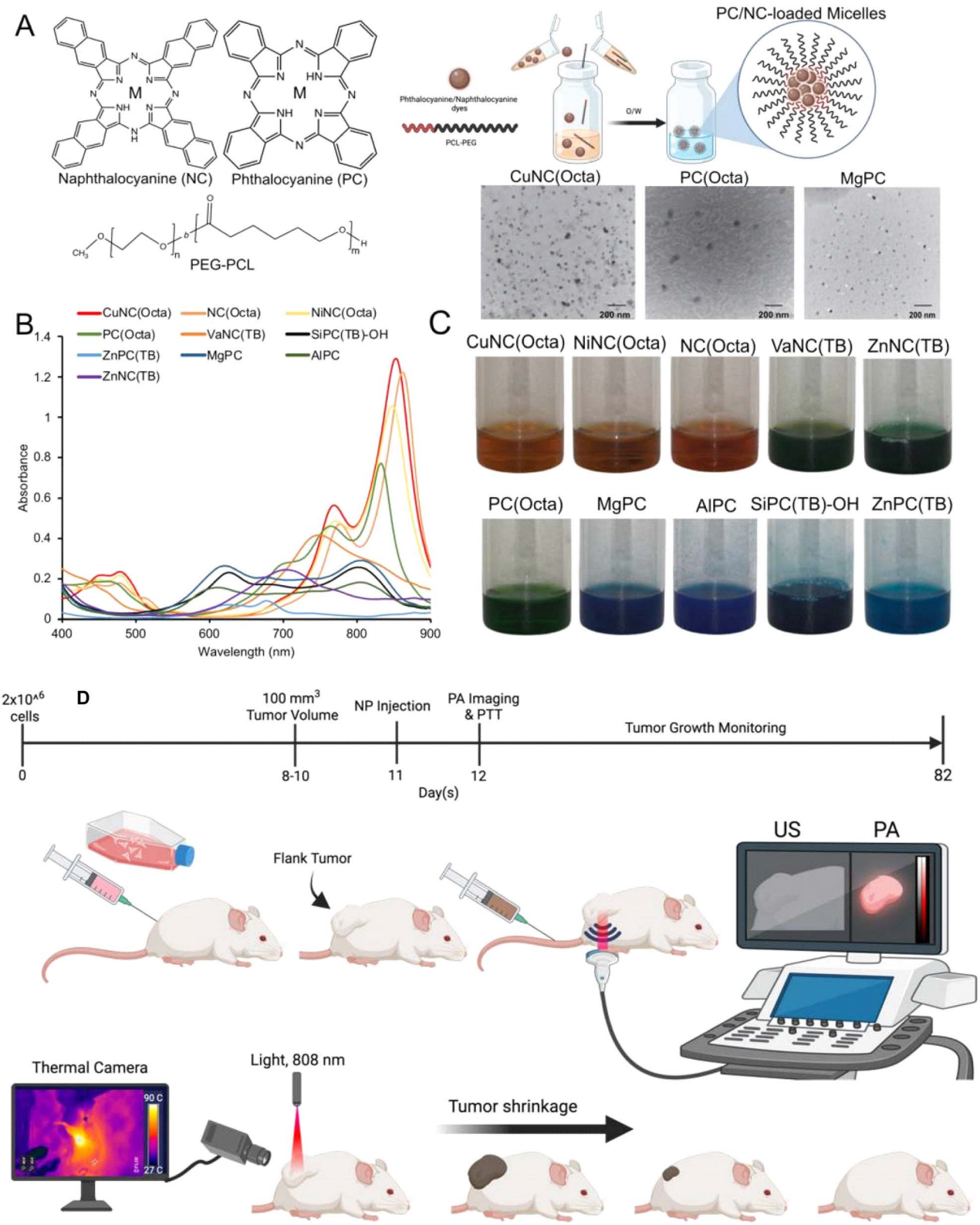

Fig. 24 (A) Schematic of NC/PC-loaded micelles formed by incorporating hydrophobic NC/PC dyes into PEG–PCL *via* oil-in-water emulsions; inset shows TEM image (scale bar: 200 nm). (B) Absorbance spectra of 10 NC/PC dyes at 10 μM. (C) Photographs of corresponding NC/PC-loaded micelle solutions in water. (D) Schematic of the animal study design showing 4T1 tumor implantation, nanoparticle administration, photoacoustic imaging, and treatment timeline in micelle-treated mice.[70]

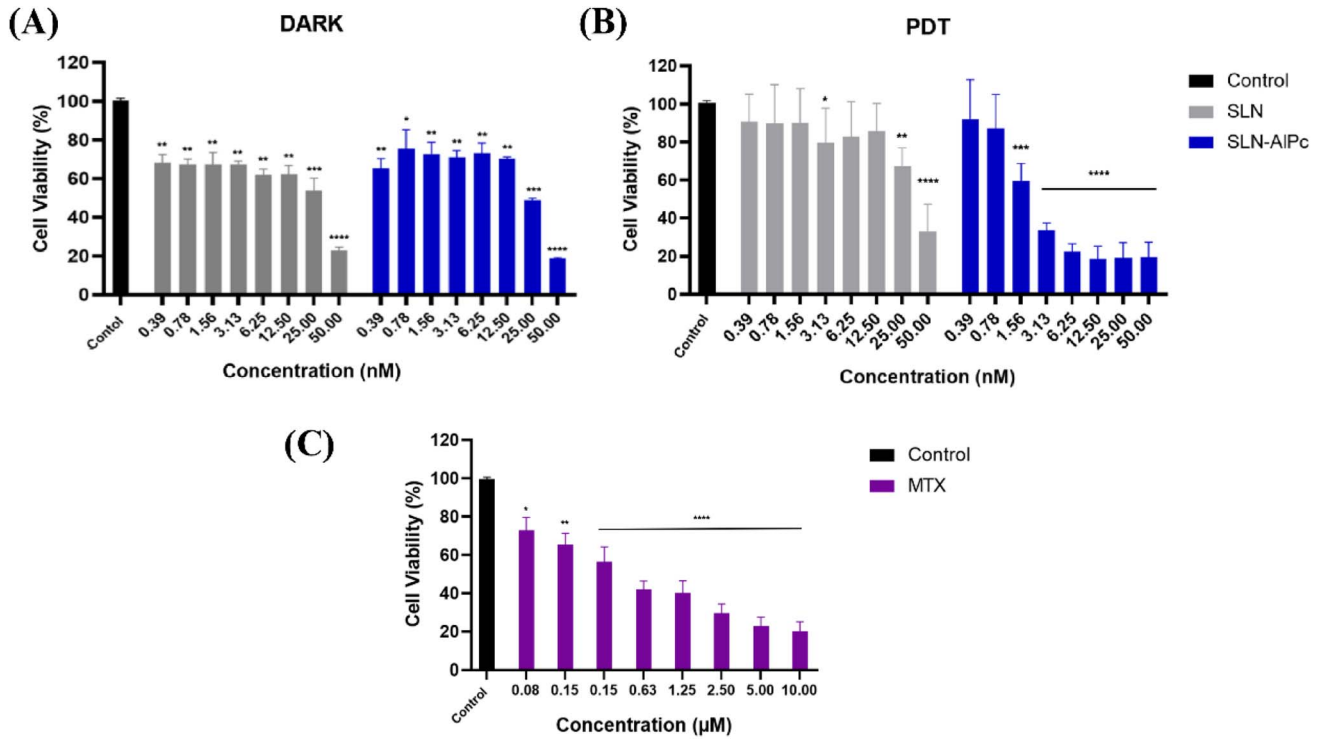

Fig. 25 MTT assay of B16–F10 cell viability after 24 h treatment: (A) SLN and SLN-AlPc; (B) PDT using SLN and SLN-AlPc; (C) mitoxantrone. Reproduced from ref. 71, under the terms of the CC BY-NC 3.0 license.

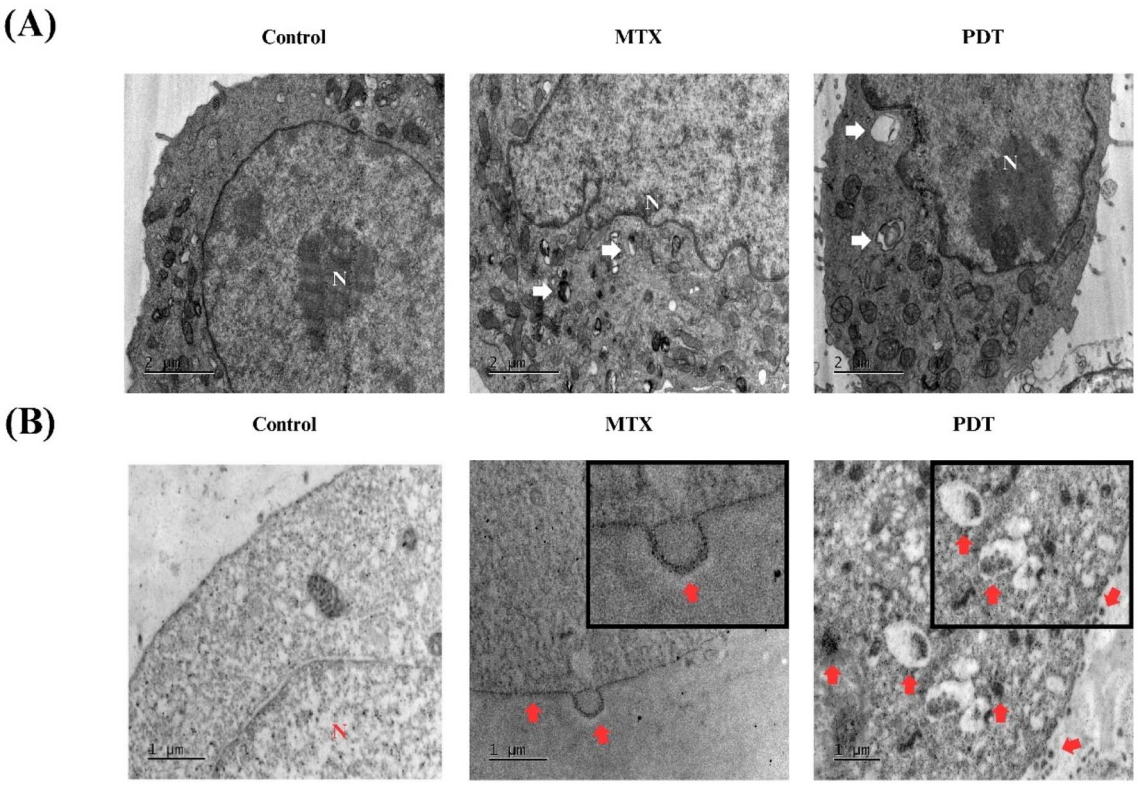

Fig. 26 TEM analysis of B16–F10 cells after 24 h treatment: (A) autophagosome formation post-PDT and MTX treatment (white arrows); (B) calreticulin immunostaining showing membrane translocation (red arrows). N: nucleus. Reproduced from ref. 71, under the terms of the CC BY-NC 3.0 license.

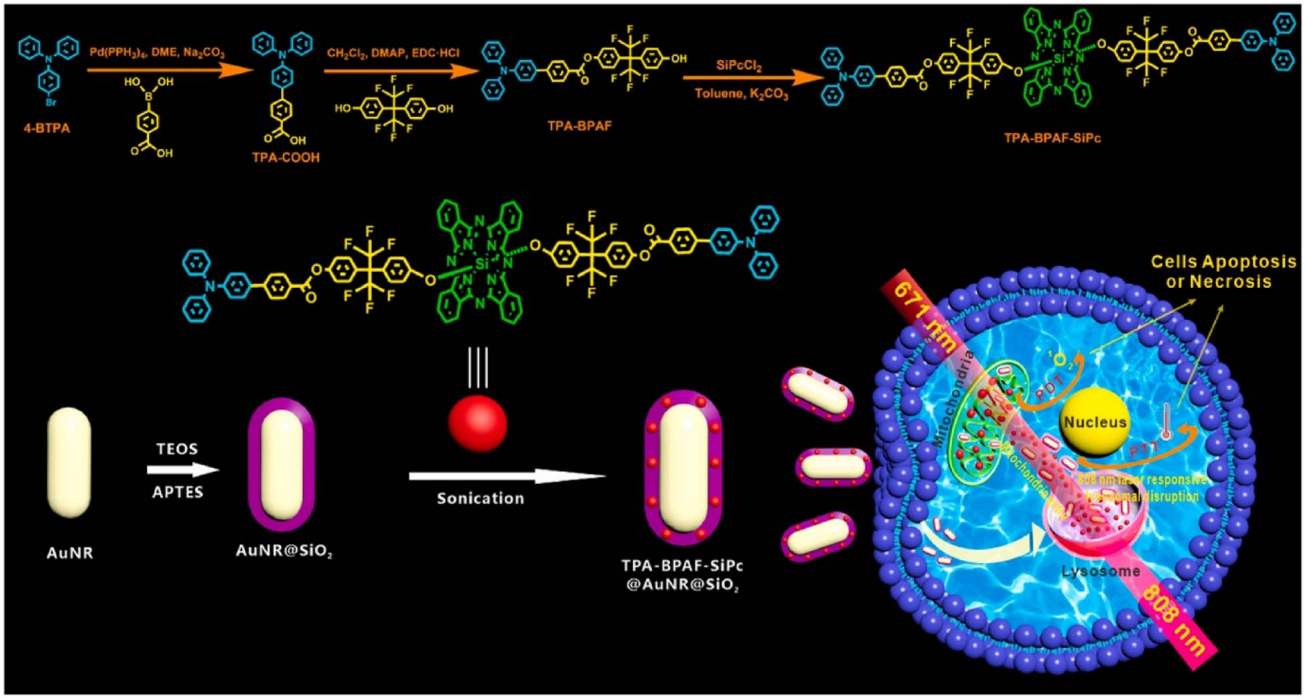

Fig. 27 Schematic of the synthesis, intracellular trafficking, and distribution of TPA-BPAF-SiPc@AuNR@SiO_2 in MCF-7 cells. Reproduced from ref. 72 with permission from Elsevier, copyright © 2025.

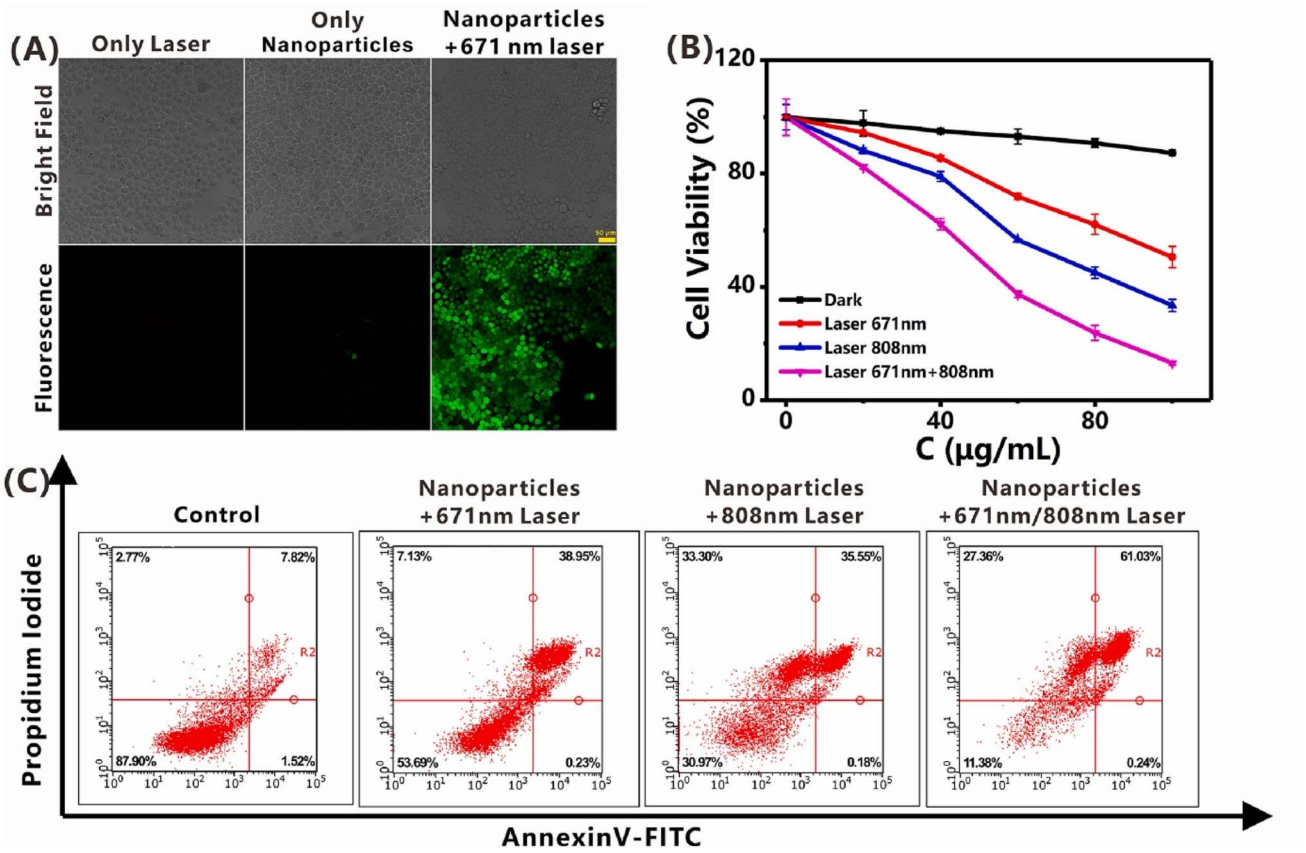

Fig. 28 *In vitro* evaluation of PDT and PTT effects of TPA-BPAF-SiPc@AuNR@SiO_2 in MCF-7 cells. (A) Confocal images showing intracellular ROS generation before and after 671 nm laser irradiation using CM-H2DCFDA probe. (B) Phototoxicity assessed by CCK-8 at varying nanoparticle concentrations. (C) Flow cytometry analysis of apoptosis following treatment with NPs and 671 nm and/or 808 nm laser irradiation. Reproduced from ref. 72 with permission from Elsevier, copyright © 2025.

induces localized hyperthermia upon irradiation, highlighting its capacity for PDT with synergistic photothermal effects. Flow cytometry analysis confirmed that the nanoparticle induces tumor cell death through both apoptotic and necrotic pathways (Fig. 28A–C). Collectively, this study highlights TPA-BPAF-SiPc@AuNR@SiO_2 as a promising candidate for two-photon fluorescence-guided photothermal-enhanced PDT, offering a targeted and effective therapeutic strategy for breast cancer treatment.[72]

Borzęcka *et al.* (2025) developed pH-responsive polymeric nanocarriers encapsulating PCs to enhance PDT efficacy in breast cancer. Among the formulations, Pc4-loaded NP (Pc4-NPs) exhibited the highest photocytotoxicity against SKBR-3 cells, with an IC_{50} of 0.021 μM—approximately fourfold more potent than free Pc4. Encapsulation improved PS solubility, cellular uptake, and selectivity, as demonstrated by TT1-NPs (Fig. 29A), which showed up to 18-fold increased activity in cell lines including PANC-1, U-251, and A549. The nanocarriers displayed high singlet oxygen quantum yields ($\Phi_\Delta = 0.56$–0.75), confirming efficient generation of ROS upon irradiation. Both free and encapsulated PSs were non-toxic in the absence of light, indicating strong photoselectivity. Fluorescence microscopy confirmed preferential accumulation of NPs in lysosomes, consistent with their pH-responsive release in the acidic tumor microenvironment (Fig. 29B). Mechanistic investigations revealed significant ROS generation contributing to oxidative stress and apoptosis. ROS levels measured in SKBR-3 cells after 12 and 24 hours incubation with free and encapsulated Ps (Pc4-NPs and TT1-NPs) showed over 100% increase compared to controls, with no significant difference between free and nanoparticle forms, indicating that encapsulation did not compromise ROS production or energy transfer. Especially, these effects were achieved at substantially lower PS doses in nanoparticle formulations (Fig. 29C). These findings demonstrate that pH-sensitive Pc-loaded NPs effectively disrupt redox balance and induce apoptotic pathways, supporting their potential as selective and potent PDT agents. Further *in vivo* studies are warranted to validate their therapeutic efficacy.[73]

Peng *et al.* (2025) introduced a novel two-photon theranostic agent, methylated quinoline silicon(IV) phthalocyanine (MQ-SiPc), designed for targeted cancer imaging and therapy. This PS undergoes intracellular self-assembly into nanofibers (SA-

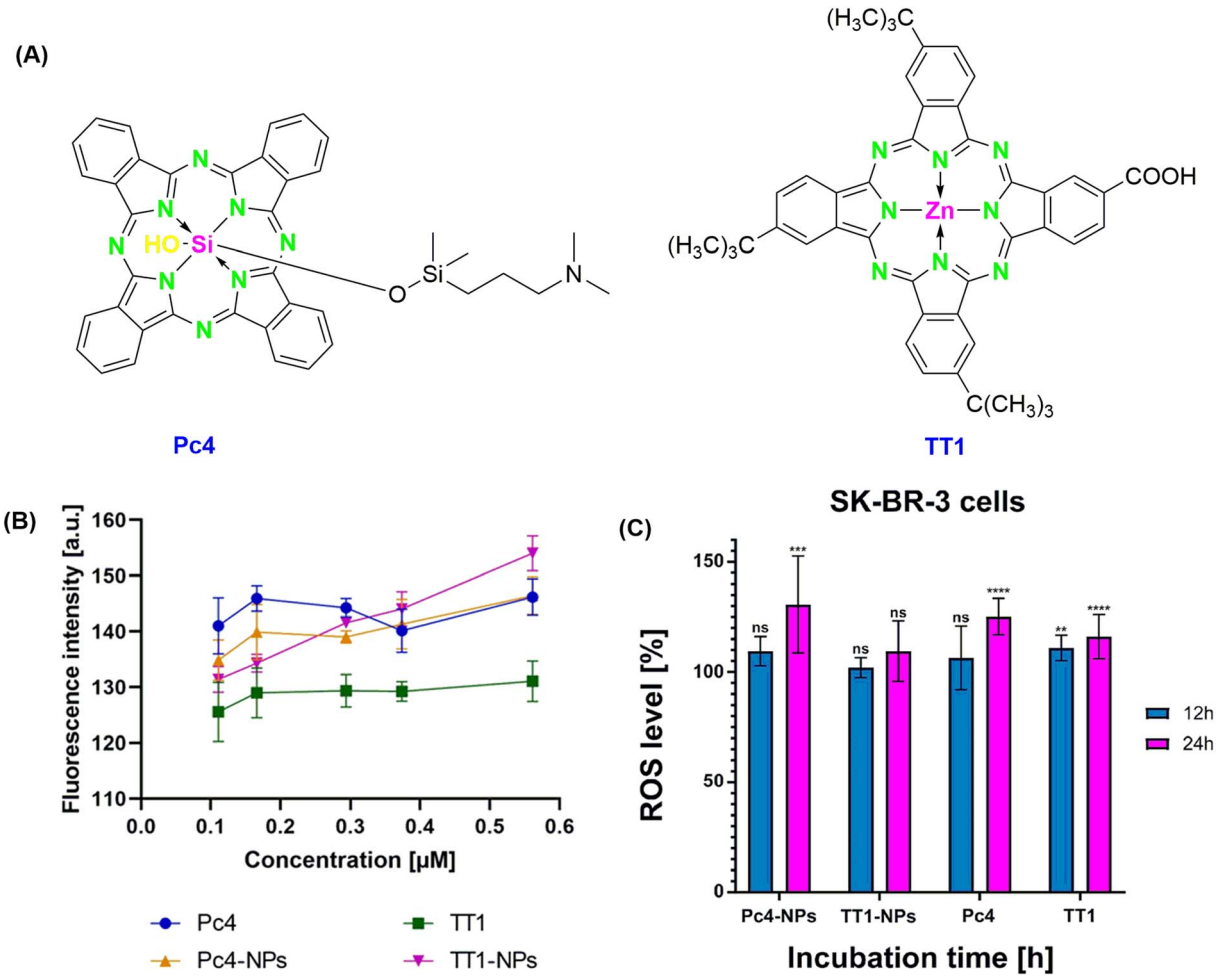

Fig. 29 (A) Chemical structure of Pc4 and TT1 (B) fluorescence intensity at 525 nm after 18 J cm^{-2} irradiation of Pc4-NPs, TT1-NPs, Pc4, or TT1 using the SOSGR probe (C) ROS levels in SK-BR-3 cells after 12 and 24 hours of treatment with Pc4-NPs, TT1-NPs, free Pc4, or TT1. Reproduced from ref. 73 with permission from Elsevier, copyright © 2025.

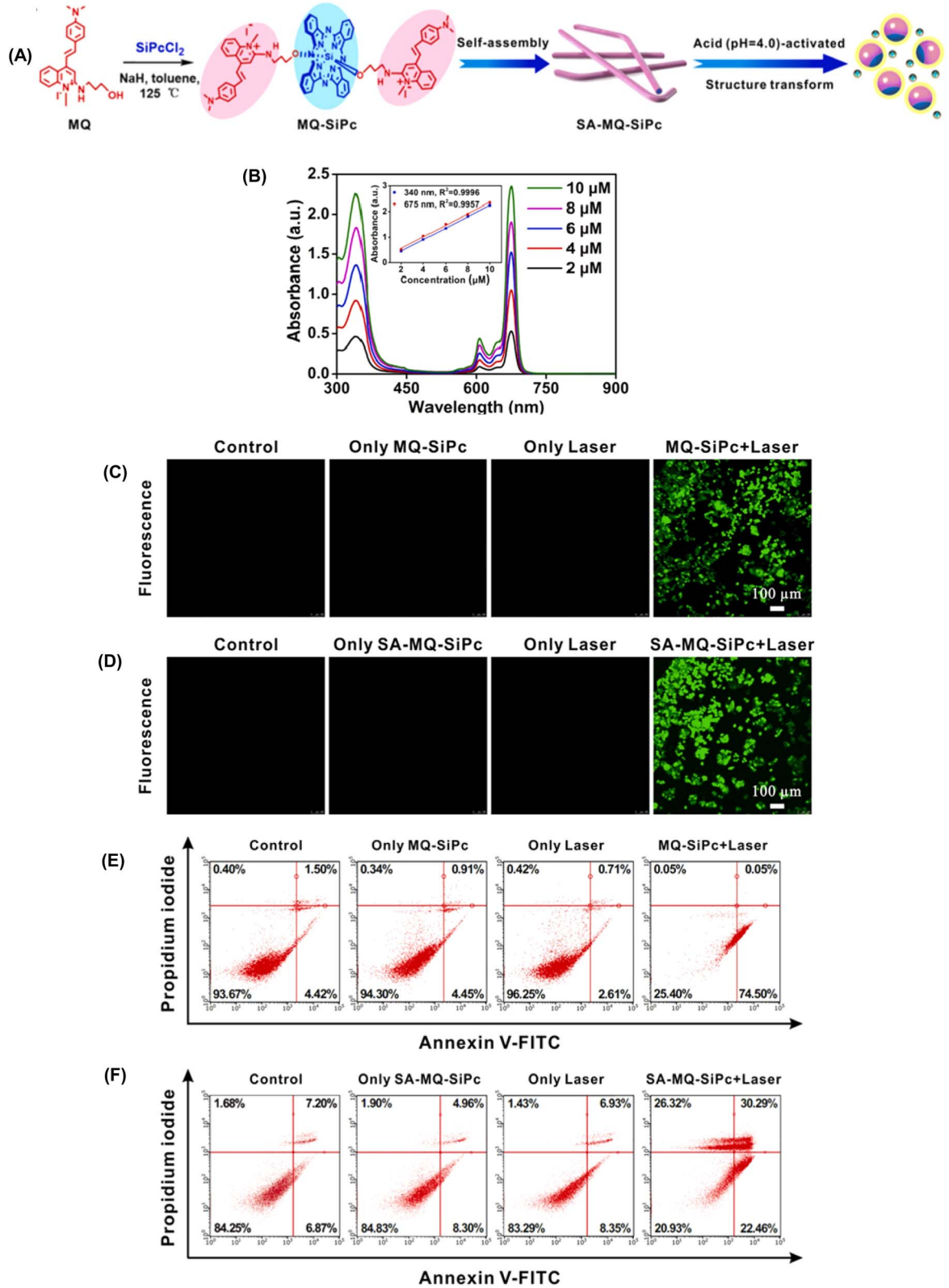

Fig. 30 (A) Synthetic pathway of MQ-SiPc, formation of nanofiber self-assemblies (SA-MQ-SiPc), and schematic illustration of its pH-dependent structural transformation (B) UV-vis absorption spectra of MQ-SiPc (4 μM) in DMSO with DPBF (60 μM) as a singlet oxygen quencher under 671 nm laser irradiation (9 mW cm^{-2}) for varying durations. Confocal fluorescence images showing ROS generation in MCF-7 cells treated with (C) MQ-SiPc and (D) SA-MQ-SiPc nanofibers (5 μM) after 671 nm laser irradiation (5 mW cm^{-2}, 5 min), using CM-H_2DCFDA as the ROS probe (λ_{ex} = 488 nm, λ_{em} = 500–530 nm) (E and F) Flow cytometry analysis of apoptosis in MCF-7 cells treated with MQ-SiPc or SA-MQ-SiPc nanofibers (5 μM) after 671 nm laser irradiation (5 mW cm^{-2}, 5 min). Reproduced from ref. 74 with permission from Elsevier, copyright © 2025.

MQ-SiPc) *via* electrostatic interactions, hydrogen bonding, and π–π stacking (Fig. 30A). These nanofibers preferentially accumulate in MCF-7 breast and BxPC-3 pancreatic cancer cells due to the EPR effect and localize within lysosomes. Within the acidic lysosomal microenvironment (pH ∼4.0), SA-MQ-SiPc nanofibers transform into fluorescent NPs, facilitating lysosome-specific imaging. Upon exposure to 671 nm laser irradiation, these structures initiate both type I and type II photoreactions, generating ROS, including superoxide radicals, along with significant photothermal effects (Fig. 30B). This dual mechanism compromises lysosomal membrane integrity, disrupts lysosomal function, and ultimately promotes tumor cell death under low-power laser conditions. ROS generation was evaluated through intracellular fluorescence imaging. As shown in Fig. 30C and D, control, laser-only, and untreated MQ-SiPc or SA-MQ-SiPc groups exhibited negligible fluorescence, indicating minimal $^1O_2$ production. In contrast, strong green fluorescence was observed in cells treated with MQ-SiPc or SA-MQ-SiPc in combination with laser irradiation, confirming efficient ROS production. To further assess the therapeutic outcome, apoptosis was analyzed using Annexin V-FITC/PI staining and flow cytometry. Non-irradiated groups displayed high viability (>83%), demonstrating low intrinsic toxicity and favorable biocompatibility. In contrast, laser-irradiated SA-MQ-SiPc-treated cells exhibited significant late apoptosis and necrosis: 30.29% and 26.32% in MCF-7 cells, and 35.66% and 30.73% in BxPC-3 cells, respectively (Fig. 30E and F). These findings validate the potent and selective photodynamic and photothermal effects of SA-MQ-SiPc, highlighting its potential for precise, *in situ* cancer theranostics.[74]

Jiang *et al.* (2025) developed a dual-functional nanosystem integrating anti-angiogenic and photodynamic modalities for enhanced oncological outcomes. By co-formulating a hydrophobic zinc phthalocyanine-based PS with monocyte-activating polypeptide-II (EMAP-II), they synthesized water-dispersible EMAP-II:PS@NPs exhibiting uniform size and high colloidal stability (Fig. 31A and B). These NP selectively targeted tumor vasculature by binding vascular endothelial growth factor receptors (VEGFR) and triggered intracellular ROS production upon NIR light exposure, leading to potent photodynamic cytotoxicity. Cellular uptake kinetics were assessed in endothelial (EA.hy 926) and cancer cell lines (HepG2 and CT26). Maximum PS accumulation occurred at 24 hours for EA.hy 926 and HepG2 cells with hEMAP-II:PS@NPs, whereas CT26 cells reached peak uptake at 8 hours using mEMAP-II:PS@NPs. EA.hy 926 cells demonstrated the highest internalization, confirming selective endothelial targeting. Upon NIR irradiation, mEMAP-II:PS@NPs-treated cells exhibited enhanced green fluorescence, indicative of elevated ROS. Subcellular distribution analysis revealed preferential PS localization within lysosomes and partial mitochondrial accumulation, with no nuclear presence, implying that lysosomal and mitochondrial damage mediate the cytotoxic response (Fig. 32A–D). Cytotoxicity assays (CCK-8) revealed minimal dark toxicity from EMAP-II:PS@NPs in all tested cell lines, unlike free PS or hEMAP-II + PS, which were toxic at higher concentrations. Under light exposure (1.5 J cm^{-2}), EMAP-II:PS@NPs induced significantly greater cell death. EA.hy 926 cells exhibited the highest sensitivity (IC_{50} = 5.3 nM), markedly lower than HepG2 and CT26 cells (>200 nM), highlighting EMAP-II's targeting efficiency. In 4T1 cells, low-dose mEMAP-II:PS@NPs (10^{-7} M) reduced viability to approximately 17.74%. *In vivo* experiments confirmed selective tumor accumulation of mEMAP-II:PS@NPs post-intravenous administration, with peak fluorescence at 6 hours. In the absence of light, moderate tumor inhibition was observed (IR = 47.63%), while NIR activation markedly enhanced efficacy (IR = 97.90%), with tumors reduced to ∼28 mm^3 by day 13. Treated animals maintained consistent body weight, and complete tumor regression occurred in some cases (Fig. 33A–J). Biodistribution studies demonstrated preferential hepatic accumulation with limited presence in other major organs. Histopathological examination showed reduced tumor cell density and vascularization in the treated group, corroborating EMAP-II's anti-angiogenic activity.[75]

Peng *et al.* (2025) reported the development of a multifunctional nano PS capable of simultaneously visualizing lipid

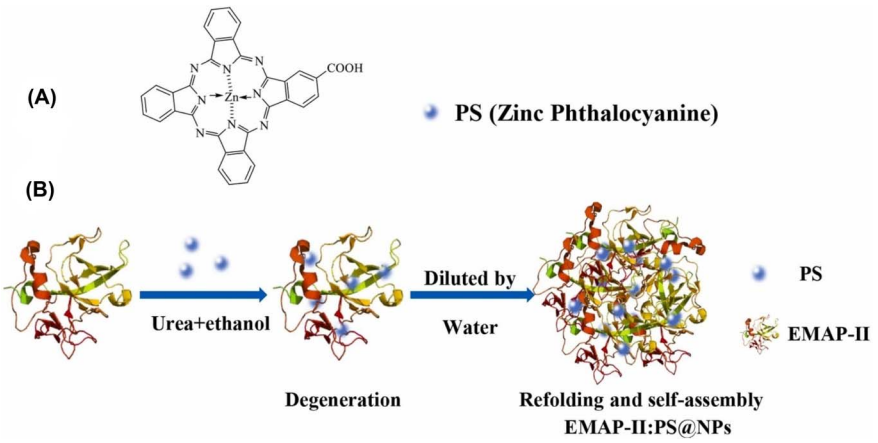

Fig. 31 (A) Chemical structure of the PS (B) schematic illustration of hEMAP-II:PS@NPs nanoparticle preparation. Reproduced from ref. 75 with permission from Elsevier, copyright © 2025.

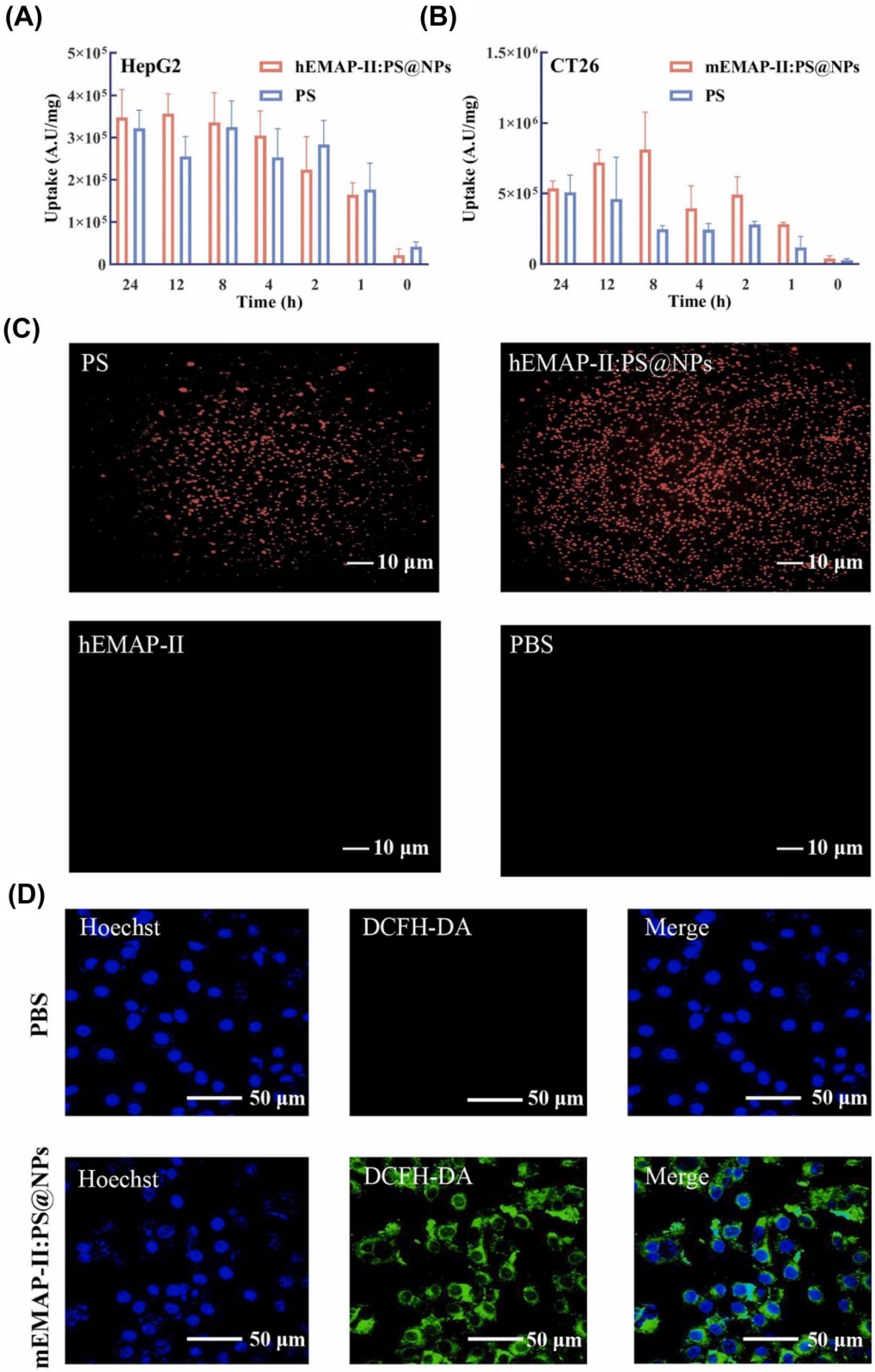

Fig. 32 Cellular uptake and ROS generation of EMAP-II:PS@NPs. (A) Uptake of hEMAP-II:PS@NPs by HepG2 cells; (B) time-dependent uptake of mEMAP-II:PS@NPs and free PS by CT26 cells; (C) uptake comparison of hEMAP-II:PS@NPs and PS in EA.hy 926 cells using high-content screening; (D) ROS generation by mEMAP-II:PS@NPs visualized *via* confocal microscopy using DCFH-DA staining. Reproduced from ref. 75 with permission from Elsevier, copyright © 2025.

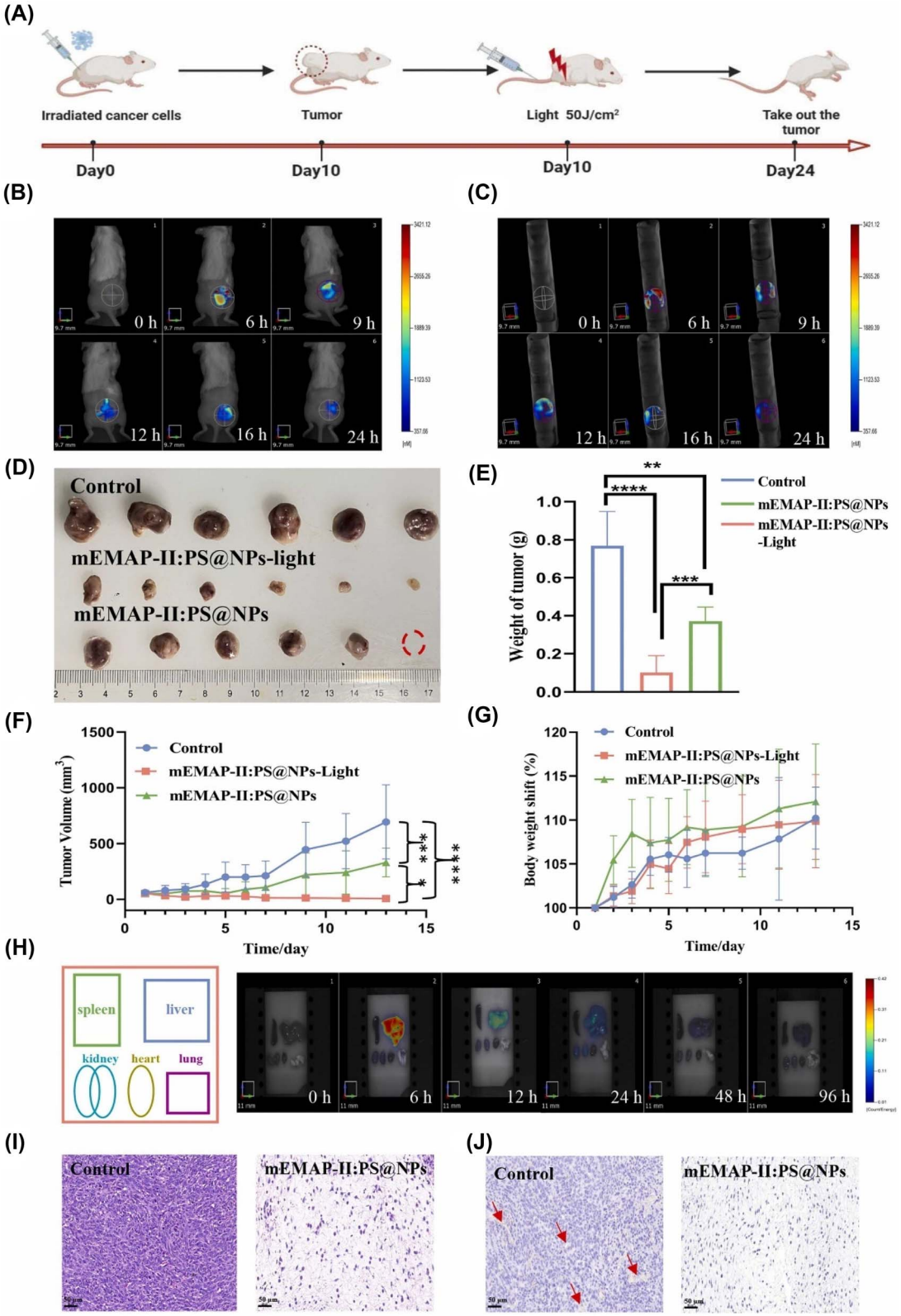

Fig. 33 Antitumor performance of mEMAP-II:PS@NPs in BALB/c mice. (A) Treatment schedule; (B) *in vivo* tumor fluorescence imaging post-injection, with tumor sites highlighted; (C) whole-body fluorescence imaging showing nanoparticle distribution; (D) tumor sizes from each group on day 13; (E) excised tumors from treated and control mice with/without light (50 J cm^{-2}); (F) tumor volume progression during treatment; (G) body weight monitoring to assess systemic toxicity; (H) biodistribution and clearance of mEMAP-II:PS@NPs in major organs over time; (I) H&E-stained tissue sections; (J) CD31 immunohistochemistry images (scale bar: 50 μm). *P < 0.05, **P < 0.01, ***P < 0.001. Reproduced from ref. 75 with permission from Elsevier, copyright © 2025.

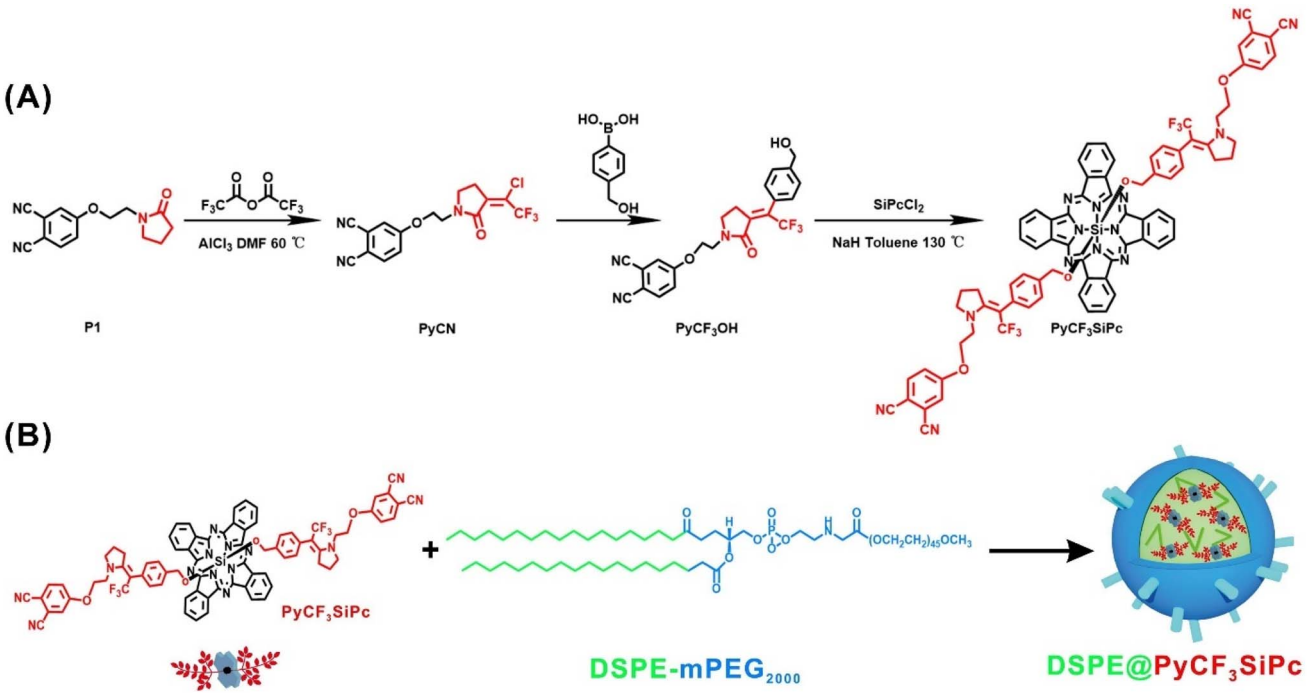

Fig. 34 (A) Synthetic route of $PyCF_3SiPc$ and (B) proposed mechanism for the self-assembly of DSPE@$PyCF_3SiPc$ NPs. Reproduced from ref. 76 with permission from Elsevier, copyright © 2025.

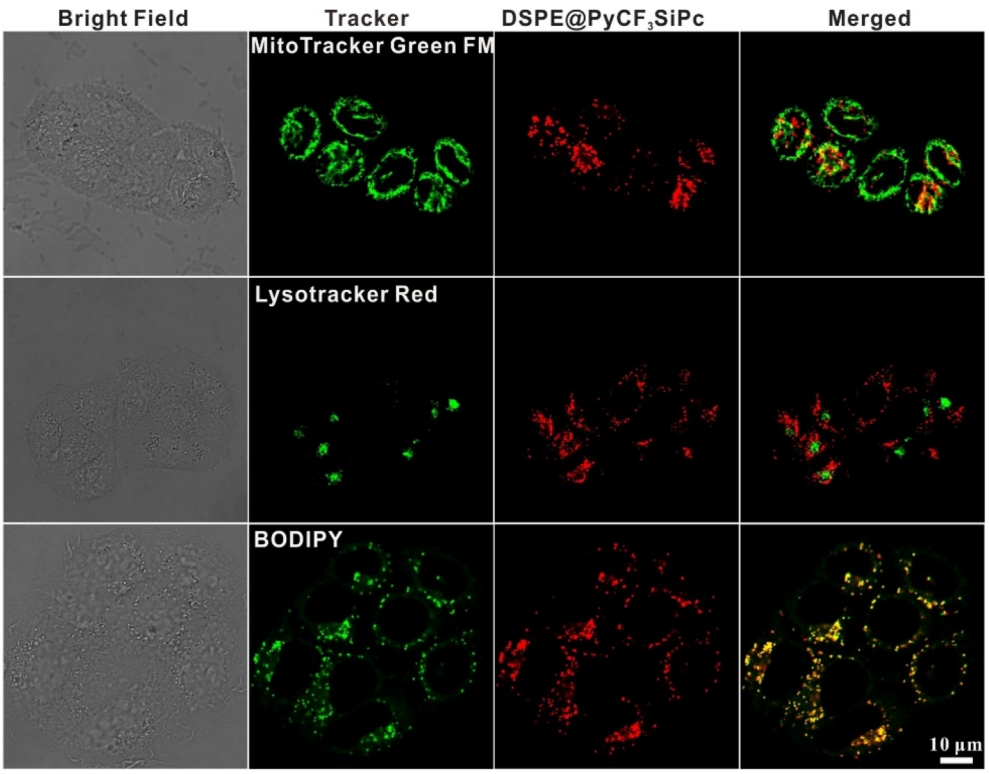

Fig. 35 Confocal microscopy images of MCF-7 cells co-stained with DSPE@$PyCF_3SiPc$ (1 μM, 4 h), MitoTracker Green, LysoTracker Red, and BODIPY, showing subcellular localization under respective excitation/emission conditions. Reproduced from ref. 76 with permission from Elsevier, copyright © 2025.

droplet (LD) dynamics and mediating PDT. The PS, a newly synthesized trifluoromethyl-pyrrolidone-substituted silicon phthalocyanine ($PyCF_3SiPc$), was structurally characterized and encapsulated into NPs using DSPE-mPEG2000 to enhance aqueous dispersibility and biocompatibility (Fig. 34A and B). The resulting DSPE@$PyCF_3SiPc$ NPs demonstrated efficient uptake by MCF-7 breast cancer cells and selective localization within LDs. These NPs exhibited strong photostability and negligible cytotoxicity in the absence of light, supporting their application in prolonged intracellular imaging. Upon laser irradiation, $PyCF_3SiPc$ emitted bright red fluorescence within LDs, which became dispersed post-illumination, indicating PDT-induced LD disruption and intracellular photochemical activity. ROS generation triggered apoptotic signaling, confirming therapeutic efficacy (Fig. 35). Cellular imaging studies using confocal laser scanning microscopy (CLSM) showed robust cytoplasmic fluorescence after 4 hours of incubation with MCF-7 cells, indicating effective membrane penetration. Subcellular localization was further analyzed through co-staining with organelle-specific fluorescent probes. Co-localization with BODIPY 493/505 yielded a Pearson's correlation coefficient (R_r) of 0.83, confirming specific accumulation in LDs. In contrast, lower R_r values were observed for Lysotracker Red (0.60) and MitoTracker Green (0.38), suggesting minimal lysosomal and mitochondrial involvement. Cytotoxicity and phototoxicity assays using MTT confirmed that DSPE@$PyCF_3SiPc$ maintained excellent biocompatibility up to 5 μM under dark conditions. However, laser exposure (670 nm, 100 mW cm^{-2} for 10 minutes) induced significant cell death, with an IC_{50} of 0.7 μM, demonstrating potent photodynamic activity (Fig. 5A). CLSM imaging further confirmed initial localization of $PyCF_3SiPc$ within LDs, with fluorescence redistribution following irradiation, indicative of LD damage and ROS-mediated photodynamic action (Fig. 36A–C).[76]

Liang *et al.* (2025) developed zinc(II) phthalocyanine NPs (ZnPcNPs) with strong near-infrared I (NIR-I) absorption and dual photothermal–photodynamic properties for cancer theranostics (Fig. 37). Under 660 nm laser irradiation, ZnPcNPs exhibited high photostability and a remarkable photothermal conversion efficiency (PCE) of 30.01%. Their strong light absorption enabled efficient heat generation and $^1O_2$ production, supporting their use for synergistic PTT and PDT.

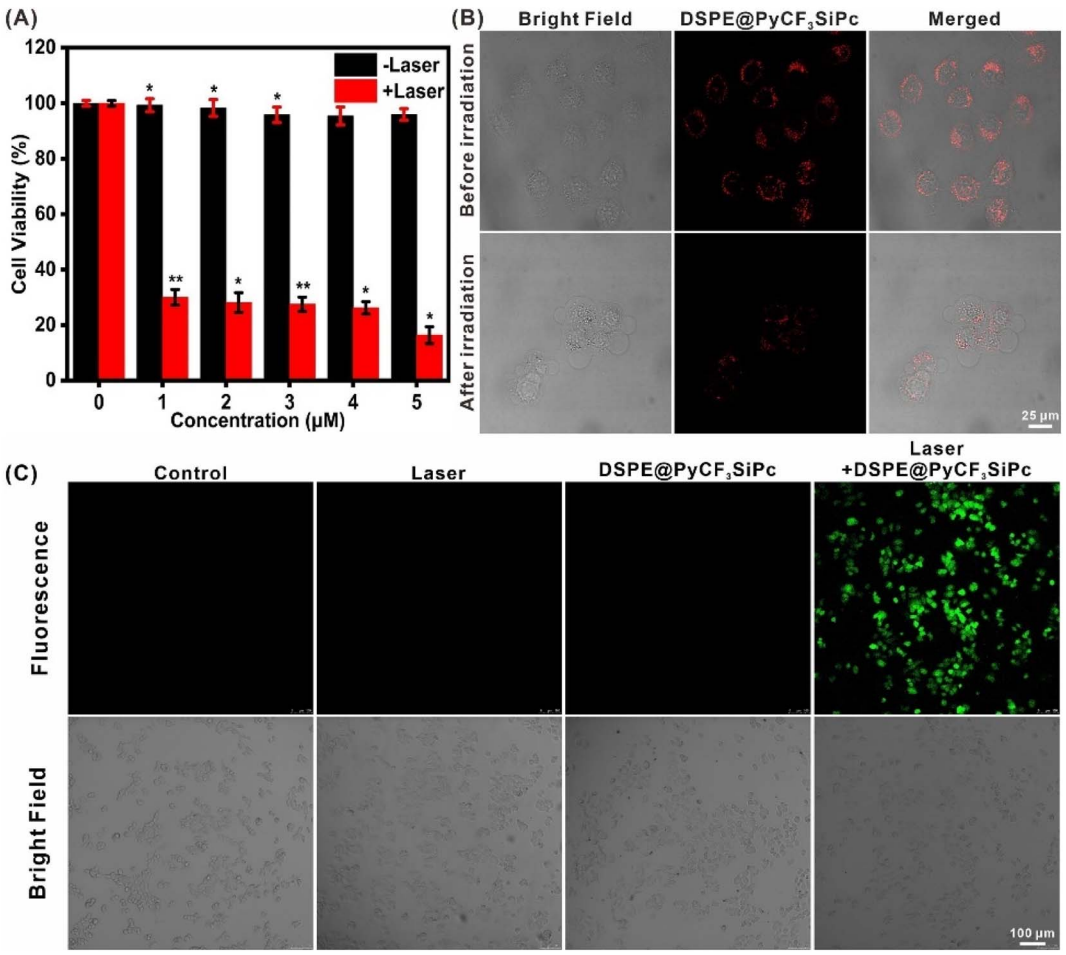

Fig. 36 (A) Cell viability of MCF-7 cells treated with DSPE@$PyCF_3SiPc$ under light irradiation (100 mW cm^{-2}, 10 min) and in the dark. (B) Confocal images of MCF-7 cells after 4 h incubation with DSPE@$PyCF_3SiPc$, captured before and after 670 nm laser irradiation (10 mW cm^{-2}, 0 and 10 min). (C) Intracellular ROS generation visualized using CM-H_2DCFDA after DSPE@$PyCF_3SiPc$ treatment and 670 nm laser exposure (100 mW cm^{-2}, 10 min). Reproduced from ref. 76 with permission from Elsevier, copyright © 2025.

Cytotoxicity was evaluated using the Cell Counting Kit-8 (CCK-8) assay in 4T1 breast cancer cells. ZnPcNPs demonstrated minimal dark toxicity, maintaining >98% cell viability across concentrations. However, upon 660 nm laser exposure (0.75 W cm^{-2}, 300 s), a concentration-dependent reduction in cell viability was observed, indicating significant photocytotoxicity *via* combined PTT and PDT mechanisms. Compared to free ZnPc, the nanoparticle formulation showed superior efficacy (Fig. 38A–D). Fluorescence-based live/dead imaging further confirmed therapeutic outcomes. Control groups (PBS, ZnPc, ZnPcNP, with or without laser) showed mostly green fluorescence (viable cells), while the ZnPc + Laser group showed partial red fluorescence (~50% dead cells). The ZnPcNP + Laser group showed extensive red fluorescence, indicating pronounced cell death, aligning with CCK-8 results. Photothermal behavior was evaluated by IR thermography. ZnPcNPs in aqueous solution (5–20 μmol L^{-1}) displayed a concentration-dependent temperature rise, reaching up to 57.2 °C after 300 s of 660 nm irradiation at 0.75 W cm^{-2}. In contrast, free ZnPc under similar conditions only reached 42.0 °C. Laser power-dependent heating (0.25–0.75 W cm^{-2}) confirmed efficient photothermal response. ZnPcNPs also showed excellent photothermal stability over five on/off cycles. The thermal relaxation method yielded a time constant (τ) of 282.19 s and a calculated PCE of 30.01% (Fig. 39A–G). *In vivo* PTT was tested in BALB/c nude mice bearing 4T1 tumors. Following intravenous ZnPcNP administration and 660 nm laser irradiation, IR imaging revealed tumor-site temperatures rising from 28.1 °C to 47.0 °C. In contrast, PBS-treated controls reached only 33.9 °C. This localized thermal effect led to effective tumor ablation exclusively in the ZnPcNP-treated group (Fig. 40A–E). ZnPcNPs demonstrate potent NIR-I responsive photothermal and photodynamic activity, with excellent biocompatibility, imaging capabilities, and therapeutic efficacy. Their superior performance over free ZnPc positions them as promising agents for dual-modality cancer therapy.[77]

7. Comparative evaluation of Pc-based photosensitizers in nanocarrier-mediated PDT

Recent advancements in Pc-based nanomedicine have revealed significant progress in PDT through the development of diverse nanocarrier systems, targeting strategies, and synergistic treatment modalities (Table 1). Across the studies summarized, zinc phthalocyanine (ZnPc) remains a central scaffold, owing to its optimal absorption in the near-infrared region (~660–700 nm), efficient generation of ROS, and compatibility with a wide array of delivery platforms.

Among the 2023 entries, Pc derivatives conjugated to gold and silver NPs demonstrated high ROS production and phototoxicity. Particularly, **Pc1** and **Pc2** embedded in glutathione-stabilized Au and Ag NP exhibited superior performance under PSDT, with AuGSH showing higher efficacy than AgGSH.

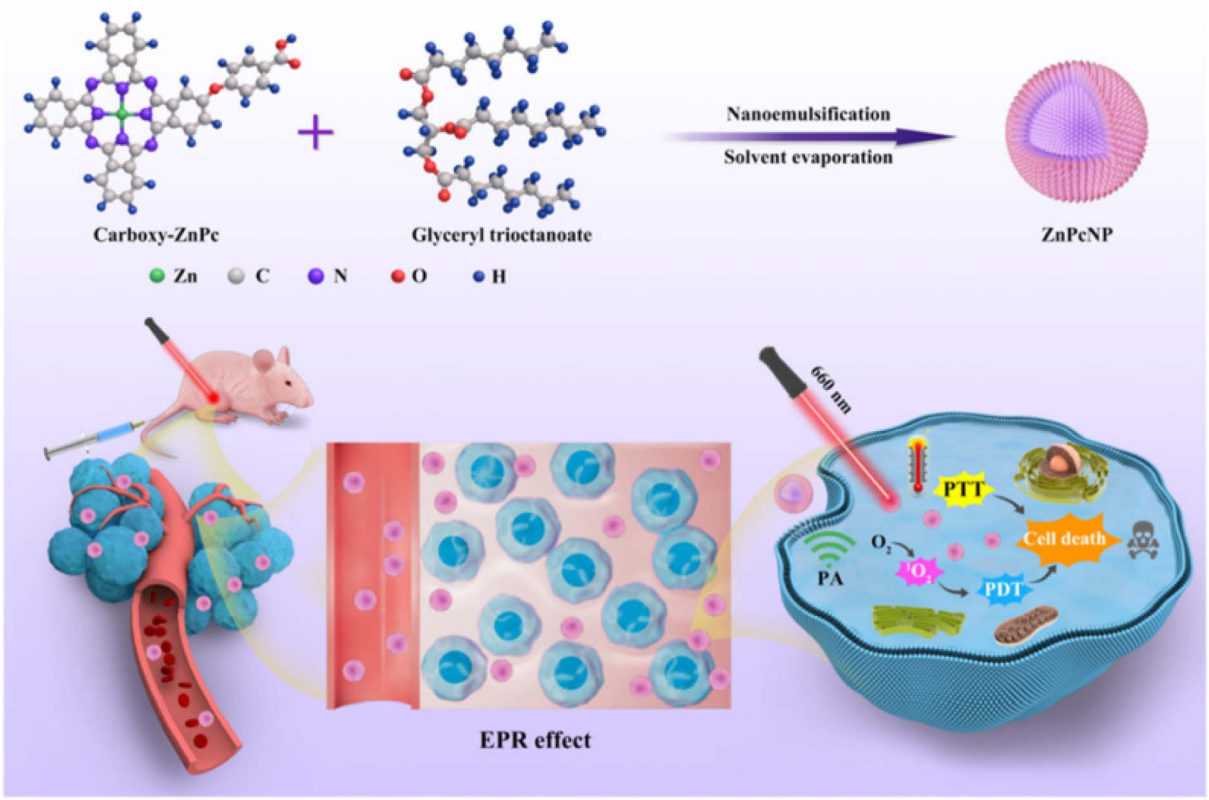

Fig. 37 Schematic of ZnPcNP synthesis and PA-guided PTT/PDT, highlighting their potential for EPR in tumors.[77]

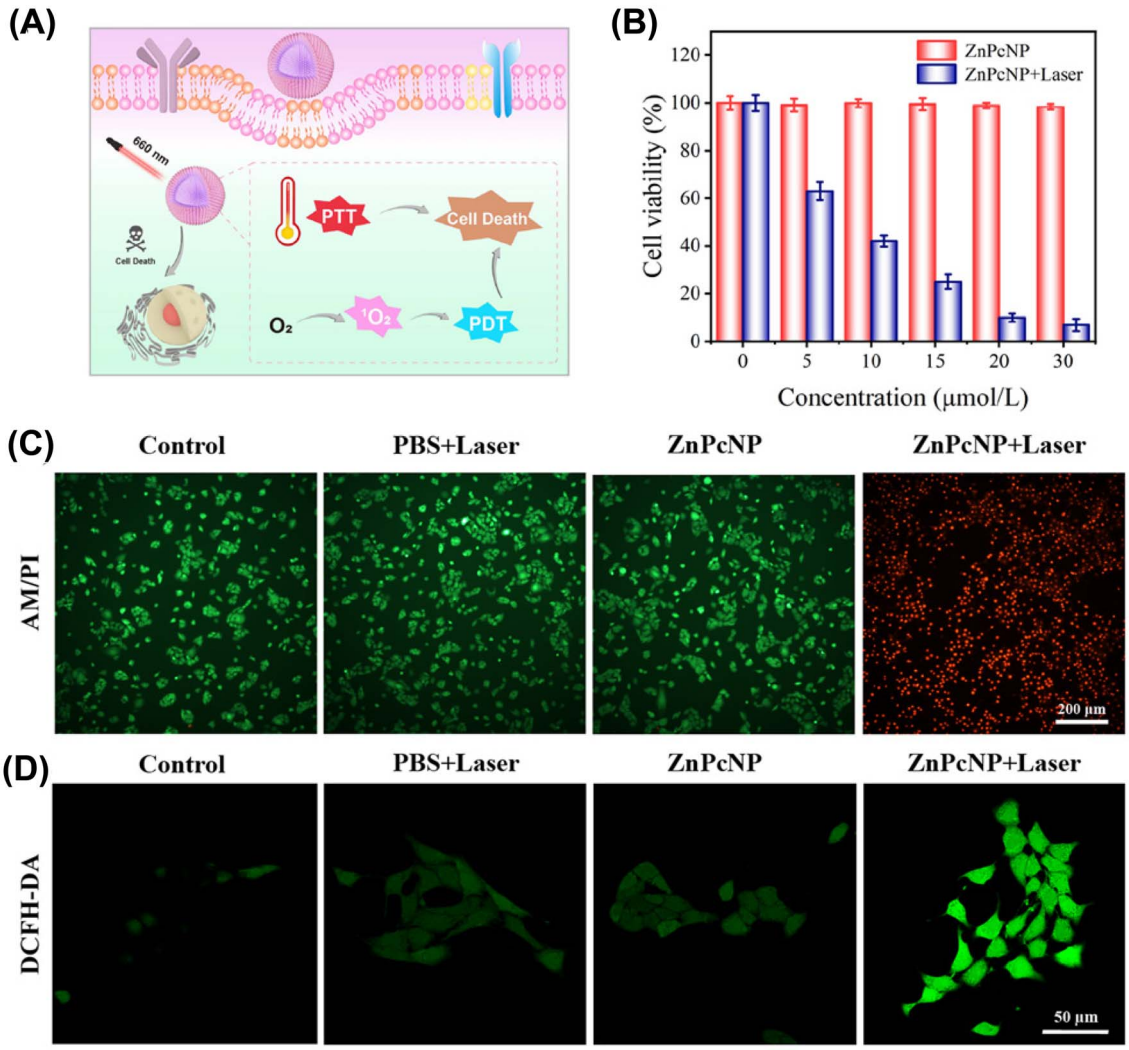

Fig. 38 Biocompatibility of ZnPcNPs: (A) schematic of synergistic PTT/PDT treatment. (B) Viability of 4T1 cells after ZnPcNP treatment with/without 660 nm laser (0.75 W cm^{-2}, 300 s) ($n = 3$). (C) Calcein-AM/PI-stained fluorescence images of treated 4T1 cells. (D) Intracellular $^1O_2$ levels in 4T1 cells detected using DCFH-DA after treatments.[77]

ZnPc integrated into boronate-linked polydopamine–Poloxamer 407 NPs achieved a dual response to acidic and oxidative conditions, highlighting the potential of stimuli-responsive release mechanisms in lung cancer models. Similarly, $ZnPcS_4$ conjugated to AuNPs markedly improved cellular uptake and induced apoptosis in melanoma spheroids, suggesting that such conjugates are favorable for deep-tissue penetration and 3D tumor models.

In 2024, multiple platforms utilizing $ZnPcS_4$ and ZnPc conjugates further improved therapeutic indices. For instance, anti-GCC- and anti-MIA-antibody-decorated AuNP–$ZnPcS_4$ conjugates achieved targeted phototoxicity in colorectal and melanoma cells, respectively. These nanobioconjugates demonstrated strong apoptotic responses in both 2D and 3D cultures, underlining the value of active targeting moieties for enhanced efficacy. Moreover, SiPc–NO hybrid systems harnessed the synergistic potential of nitric oxide (NO) and PDT, leading to significant suppression of cancer cell migration and improved safety profiles.

Aluminium-based Pc derivatives, such as $AlPcS_4Cl$ and AlPc in solid lipid NPs (SLNs), also showed promising outcomes by inducing ICD and DNA double-strand breaks (DSBs), extending the therapeutic implications beyond direct tumor ablation to immune modulation. Furthermore, polymeric micelles encapsulating Cu-based naphthalocyanine (CuNC(Octa)) provided strong photothermal conversion under 870 nm excitation, enabling dual imaging and therapy in triple-negative breast cancer.

In 2025, cutting-edge designs integrated mitochondrial and lysosomal targeting strategies with advanced delivery systems. The TPA-BPAF-SiPc encapsulated in silica-coated gold nanorods achieved subcellular targeting and dual PDT/PTT activity, reflecting a shift towards multi-modal precision therapy. Likewise, MQ-SiPc formed intracellular self-assembled nanofibers in acidic environments, combining pH-sensitive delivery with

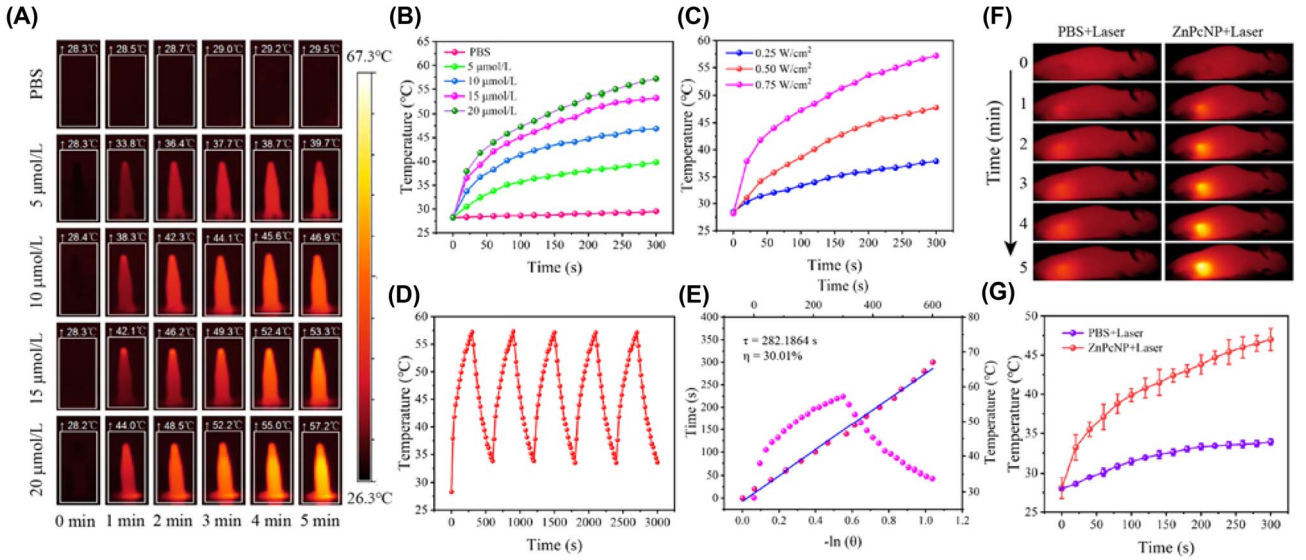

Fig. 39 *In vitro* and *in vivo* photothermal responses of ZnPcNPs: (A) IR thermal images of PBS and ZnPcNPs (5–20 μM) under 660 nm laser irradiation. (B) Corresponding photothermal heating curves. (C) Temperature profiles of 20 μM ZnPcNPs irradiated at different laser powers (0.25–0.75 W cm^{-2}). (D) Photothermal stability over five laser on/off cycles. (E) Thermal relaxation curve and time constant (τ) for one on/off cycle. (F) IR thermographic images of 4T1 tumor-bearing mice post intravenous injection of PBS or ZnPcNPs under 660 nm laser. (G) Tumor temperature elevation during *in vivo* photothermal treatment.[77]

dual ROS generation pathways (Type I and II). Pc4 formulated in pH-responsive NPs yielded high singlet oxygen quantum yields (Φ_Δ = 0.56–0.75), underlining its strong PDT potency. ZnPc combined with PROTAC LST-4 NPs in hepatocellular carcinoma cells effectively merged PDT with glutathione depletion and chemotherapy, supporting the rationale for combination therapies.

Additionally, the ZnPc-based nanoplatform with EMAP-II targeting VEGFR displayed broad antitumor efficacy across multiple cancer types and vascular endothelial cells, integrating anti-angiogenic properties with PDT—an approach that may significantly impair tumor vasculature alongside direct cytotoxicity.

Considering overall photophysical performance, therapeutic efficacy, tumor selectivity, and functional versatility, the most promising systems include:

- **Pc1**/**Pc2**@AuGSH for its multi-modal PSDT action and high ROS yield,
- ZnPcS4–AuNP–antibody conjugates for target-specific cytotoxicity in 3D tumor models,
- EMAP-II–ZnPc NPs for combining PDT with anti-angiogenic therapy, and
- MQ-SiPc for its dual-mode ROS production, subcellular self-assembly, and effective PDT/PTT synergy.

These results collectively indicate that rational design integrating targeted delivery, responsive release mechanisms, and dual-functionality (*e.g.*, PDT + PTT or NO release) can significantly augment the therapeutic impact of PCs. Among the entries analyzed, EMAP-II-functionalized ZnPc NPs and MQ-SiPc nanofibers emerge as the most comprehensive systems, offering high efficacy across tumor models, ROS generation pathways, and auxiliary therapeutic mechanisms.

8. Mechanism of improved photodynamic efficiency

The incorporation of nanoparticles with Pc PSs has emerged as a powerful strategy to significantly enhance the overall efficiency of PDT (Fig. 41). One of the major challenges associated with conventional Pcs is their intrinsic hydrophobicity, which limits their solubility in aqueous environments and hampers effective biodistribution. The use of nanoparticle carriers addresses this limitation by improving the aqueous solubility and stability of hydrophobic MPcs, facilitating their systemic administration and favorable pharmacokinetics.

Another critical advantage provided by nanoparticle conjugation is the prevention of PS aggregation. In solution, MPcs have a strong tendency to aggregate through π–π stacking interactions, which significantly quenches their excited states and diminishes the generation of ROS. Nanoparticle encapsulation or surface attachment effectively suppresses this aggregation, maintaining the monomeric form of the PS and thereby preserving its photodynamic activity.

Furthermore, nanoparticles can promote preferential accumulation of the PS at the tumor site through both passive and active targeting mechanisms. Passive targeting is achieved *via* the EPR effect, where the leaky vasculature and poor lymphatic drainage of tumors enable nanoparticles to concentrate selectively within tumor tissues. Active targeting can be accomplished by functionalizing the nanoparticle surface with ligands, antibodies, or peptides that specifically recognize and bind to tumor-associated markers, thus further enhancing the selectivity and uptake of the PS by cancer cells.

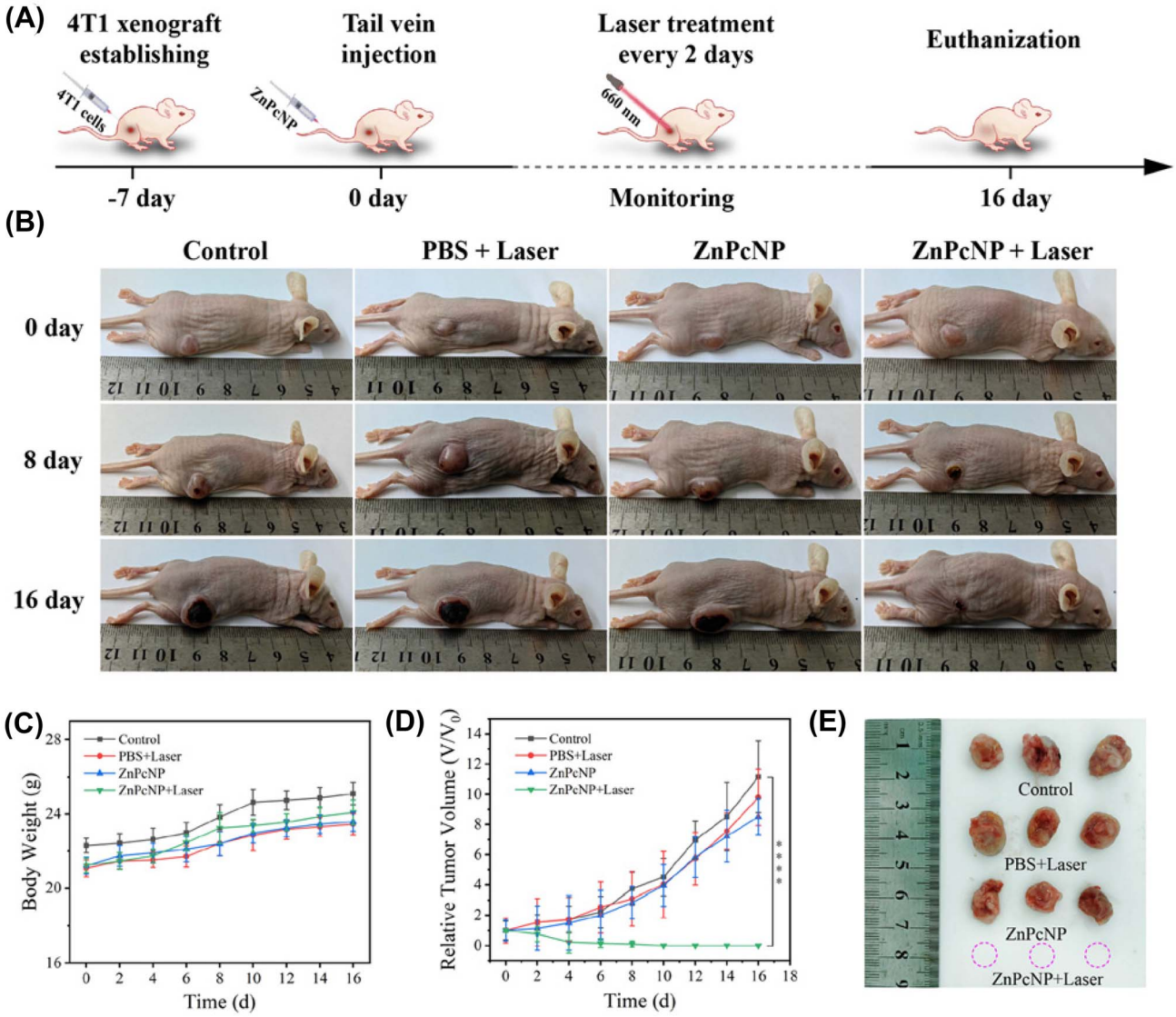

Fig. 40 *In vivo* tumor eradication by ZnPcNP-mediated PTT/PDT in 4T1 tumor-bearing BALB/c mice: (A) experimental timeline showing tumor establishment and 16-day treatment with intravenous ZnPcNPs (5 mg kg^{-1}). (B) Representative images of mice from control, 'PBS + Laser', ZnPcNP, and 'ZnPcNP + Laser' groups. (C and D) Body weight (C) and tumor volume (D) changes over 16 days (****$p < 0.0001$, $n = 3$). (E) Excised tumors on day 16.[77]

In addition, nanoparticle-based systems can enable controlled and stimuli-responsive release of Pc molecules. For instance, some nanoparticle formulations are designed to release their cargo upon exposure to specific triggers such as pH changes, enzymatic activity, or light irradiation. This ensures that the activation and release of the PS occur precisely at the tumor site, minimizing systemic toxicity and off-target side effects while maximizing therapeutic outcomes.

Henceforth, the integration of NPs with Pc PSs not only addresses the physicochemical limitations of the free PS but also introduces new functionalities that significantly elevate the precision, efficacy, and safety of PDT. Continued advances in nanoparticle design and functionalization are expected to further optimize these synergistic effects, paving the way for more effective and clinically translatable PDT platforms.

9. Challenges and limitations

Despite the growing interest and promising outcomes associated with nanoparticle-assisted Pc-PDT, several challenges and limitations hinder its clinical translation and therapeutic efficacy. These include:

- Biocompatibility and toxicity: the long-term biocompatibility and potential cytotoxicity of certain NPs remain a major concern. Some inorganic NPs, such as quantum dots or metal-based carriers, may induce oxidative stress, inflammation, or off-target effects.
- Pharmacokinetics and biodistribution: achieving controlled biodistribution and prolonged circulation time is difficult. NPs may accumulate in the liver and spleen due to the

Table 1 Summary of recent advancements (2023–2025) in Pc-based PSs for nanocarrier-assisted PDT

Year	Photosensitizer (PS)	Nanocarrier type	Targeting moiety	Cancer type	$\lambda_{abs}/\lambda_{em}$ (nm)	ROS generation	PDT outcome	Reference
2023	**Pc1** (Me), **Pc2** (Et)	AuGSH and AgGSH NPs	None	Breast (MCF-7)	~670 (light + US)	Very high ($^1O_2$, $^{\cdot}OH$ *via* PSDT)	Enhanced PDT, SDT, and highest efficacy in PSDT; AuGSH > AgGSH	59
2023	ZnPc	Boronate-linked polydopamine–Poloxamer 407 NPs	None (suggested ligand mod)	Lung (A549)	~660	High under acidic/ROS conditions	73.5% cell inhibition at 5 μg mL^{-1}; pH & ROS-responsive release; dual PDT/PTT	60
2023	AlClPcTS41	PEGylated Cu–Au bimetallic nanoparticles	None (PEGylation)	Colorectal (Caco-2)	636/~670	Efficient ROS	Enhanced uptake and ROS; greater phototoxicity; low dark toxicity	57
2023	$ZnPcS_4$	Gold nanoparticles (AuNPs)	None	Melanoma (A375 spheroids)	~670/~700	High	Improved cellular uptake; apoptosis induction; increased phototoxicity *vs.* free $ZnPcS_4$	61
2023	Pc derivatives (Zn, Co, Mn)	Silver nanoparticles (AgNPs) functionalized with carbazole-substituted phthalonitrile	None	Lung (A549), colon (DLD-1), normal (WI38)	~670/~700	Moderate to high	Selective phototoxicity; dose-dependent cytotoxicity; superior to cisplatin in some cells	62
2024	SiPc–NO	Self-assembled nanoparticles (NPs)	RGD peptide	4T1 (breast), MCF-7 (breast)	Not specified	Enhanced (NO + PS)	Significant inhibition of cell migration (2.18× in 4T1, 4.21× in MCF-7); enhanced antitumor efficacy and safety	63
2024	Triphenylphosphine-labeled Pc	Complex with BSA and AuNPs	None specified	A375 melanoma	Not specified	$\Phi_\Delta = 0.47$ in DMF	Superior photodynamic efficacy *vs.* free Pc; reduced viability to 23.1% *vs.* 48.7%	64
2024	ZnPc	Periodic mesoporous organosilica (PMO)	None specified	4T1 tumor-bearing mice	Not specified	Enhanced singlet oxygen generation	Significant tumor growth suppression *in vivo*; maintained biocompatibility	65
2024	ZnPc tetrasulfonic acid ($ZnPcS_4$)	AuNP conjugate with anti-MIA antibody	Anti-MIA monoclonal antibody	A375 melanoma	Not specified	pH-responsive release; ROS elevated	Marked cytotoxicity; strong apoptotic response in 2D and 3D cultures; highest efficacy with nanobioconjugate (NBC)	66
2024	$ZnPcS_4$	AuNP conjugate with anti-GCC antibody	Anti-GCC antibody	Caco-2 colorectal cancer	Not specified	Enhanced ROS upon irradiation	Strong apoptosis induction in 2D and 3D spheroids; higher PS dose needed for 3D; promising *in vivo* translation	67

Table 1 (*Contd.*)

Year	Photosensitizer (PS)	Nanocarrier type	Targeting moiety	Cancer type	$\lambda_{abs}/\lambda_{em}$ (nm)	ROS generation	PDT outcome	Reference
2024	Aluminium phthalocyanine chloride ($AlPcS_4Cl$)	Free or PDT treatment	None	Oesophageal cancer	Not specified	Elevated ROS; DNA damage (DSBs)	Cell cycle arrest, apoptosis activation; no autophagy induction	68
2024	Zinc phthalocyanine (ZnPc) (co-loaded)	PROTAC LST-4 nanoparticles	None	HepG2 hepatocellular carcinoma	Not specified	ROS generation amplified	Synergistic tumor suppression combining chemotherapy, GSH depletion, and PDT	69
2024	Naphthalocyanine (CuNC(Octa))	PEG-PCL polymeric micelles	None	4T1 triple-negative breast cancer	~870 nm absorbance	High photothermal conversion	Effective photoacoustic imaging and photothermal therapy; complete tumor eradication	70
2024	Aluminium phthalocyanine (AlPc)	Solid lipid nanoparticles (SLN-AlPc)	None	B16–F10 melanoma	Not specified	Increased ROS	Induced immunogenic cell death (ICD), dendritic cell activation, proinflammatory cytokine secretion	15
2025	TPA-BPAF-SiPc	AuNR@SiO_2 (gold nanorods in silica)	Mitochondrial targeting post lysosomal escape	Breast cancer	Not specified/ two-photon fluorescence	Yes (efficient)	Dual (PDT + PTT)	72
2025	Pc4	pH-responsive polymeric nanoparticles	Passive (EPR effect + lysosomal release)	Breast (SKBR-3), others (PANC-1, U-251, A549)	Not specified	Yes ($\Phi_\Delta = 0.56$–0.75)	PDT	73
2025	MQ-SiPc (methylated quinoline SiPc)	Intracellular self-assembled nanofibers	Lysosome-targeting *via* pH-triggered self-assembly	Breast (MCF-7), pancreatic (BxPC-3)	671/green fluorescence (ROS)	Yes (type I and II)	Dual (PDT + PTT)	74
2025	Zinc(II) Pc (with EMAP-II)	EMAP-II:PS@NPs (water-dispersible nanoparticles)	VEGFR-targeted (*via* EMAP-II)	Hepatocellular (HepG2), colon (CT26), breast (4T1), endothelial (EA.hy 926)	NIR (not exact λ given)	Yes	PDT + anti-angiogenesis	75
2025	$PyCF_3SiPc$	DSPE-based NPs	None	Breast (MCF-7)	830 (2P)/650–700	High	Efficient mitochondrial localization and phototoxicity	76
2025	ZnPc	ZnPcNPs (NIR-I absorbing)	Passive (EPR effect)	Breast (4T1)	660/NIR-I	Yes ($^1O_2$)	Dual (PDT + PTT)	77

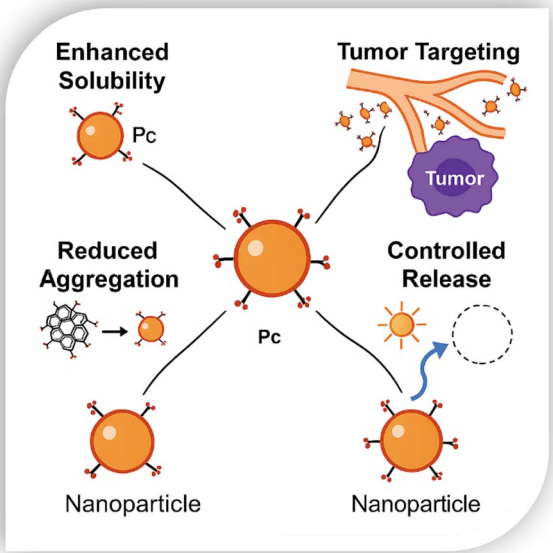

Fig. 41 Enhanced photodynamic efficiency achieved through nanoparticle integration.

mononuclear phagocyte system, reducing tumor-targeting efficiency.

• Tumor targeting and penetration: while NPs enhance passive targeting *via* the EPR effect, heterogeneous tumor vasculature and elevated interstitial pressure can limit effective penetration and uniform distribution within the tumor microenvironment.

• Photoactivation limitations: the limited tissue penetration depth of light required to activate phthalocyanine PSs restricts treatment efficacy, particularly in deep-seated tumors.

• Scalability and reproducibility: the synthesis of nanoparticle-PS conjugates often involves complex, multi-step procedures that can be challenging to reproduce on a large scale with consistent quality.

• Regulatory and translational barriers: stringent regulatory requirements for nanoparticle-based therapeutics and the lack of standardized evaluation protocols delay clinical approval and commercial development.

Overcoming these limitations requires interdisciplinary efforts in materials science, photochemistry, pharmacology, and clinical research to optimize the design, delivery, and therapeutic index of nanoparticle-assisted Pc-PDT systems.

10. Future perspectives

Pcs have demonstrated remarkable potential in PDT, yet several avenues remain for further improvement and clinical translation. Future research will likely focus on the rational design of next-generation Pc derivatives with enhanced photophysical properties, including higher singlet oxygen quantum yields, greater photostability, and improved solubility in physiological environments. Engineering PSs that can be activated by longer wavelengths within the near-infrared (NIR-II) window (1000–1700 nm) would enable even deeper tissue penetration, broadening the range of treatable tumors.

The integration of Pcs with nanotechnology presents another promising frontier. Nanocarrier systems such as liposomes, polymeric NPs, metal–organic frameworks (MOFs), and inorganic NPs can be employed to improve targeted delivery, reduce systemic toxicity, and overcome issues related to aggregation and poor aqueous solubility. Smart, stimuli-responsive nanocarriers that release the PS in response to tumor-specific microenvironmental cues—such as pH, enzymes, or redox conditions—could further enhance therapeutic precision.

Another emerging area involves the development of multifunctional platforms combining PDT with other therapeutic modalities, such as chemotherapy, immunotherapy, and PTT. Such combinatorial strategies may synergistically enhance antitumor efficacy and address limitations like hypoxia within the tumor microenvironment, which often impairs PDT outcomes.

Furthermore, efforts are needed to understand and manipulate the immunological effects of PDT. Recent findings suggest that PDT can initiate ICD, leading to systemic antitumor immune responses. Designing Pc-based systems that can potentiate these immune responses offers exciting opportunities for cancer vaccination and metastasis control.

Finally, translating Pc-based systems into clinical settings will require extensive *in vivo* studies, comprehensive toxicological evaluations, and scalable, reproducible synthesis protocols compliant with regulatory standards. Collaboration between chemists, biologists, material scientists, and clinicians will be critical to accelerating the development of safe, efficient, and patient-tailored photodynamic therapies.

11. Conclusions

Recent progress in nanoparticle-mediated delivery of phthalocyanine (Pc)-based PSs has significantly enhanced the efficacy and precision of PDT in cancer treatment. The integration of diverse nanocarrier systems—including gold, silver, mesoporous silica, solid lipid, polymeric micelles, and self-assembled nanostructures—has enabled improved solubility, tumor targeting, subcellular localization, and photostability of Pc derivatives. These platforms facilitate both passive and active targeting strategies, such as EPR effects, ligand-directed tumor homing, and pH/ROS-responsive release, thereby maximizing PS accumulation in malignant tissues while minimizing off-target toxicity. Moreover, the conjugation of targeting ligands (*e.g.*, RGD peptides, antibodies, or mitochondrial localization motifs) has led to superior cellular uptake and subcellular precision, improving ROS production and phototoxic response. Several studies highlight the dual or multimodal therapeutic potential of Pc-nanoconjugates, combining PDT with photothermal therapy (PTT), sonodynamic therapy (SDT), chemotherapy, or immunotherapy. Such synergistic approaches have demonstrated significant tumor regression, especially in three-dimensional spheroids and *in vivo* models, while maintaining biocompatibility and reduced dark toxicity. The use of NIR light,

including two-photon activation and NIR-I absorbing platforms, has further expanded the treatment window, allowing deeper tissue penetration and real-time imaging capabilities. Especially, some Pc-based systems have shown promise in inducing ICD and inhibiting angiogenesis, suggesting potential for systemic anticancer effects beyond local tumor ablation. In conclusion, phthalocyanine-loaded nanoplatforms represent a versatile and rapidly evolving class of phototherapeutics with broad potential across various cancer types. Continued development focusing on tumor-specific delivery, controlled release mechanisms, and integration with multimodal therapeutic strategies will be key to advancing these systems toward clinical translation.

Author contributions

Nafeesa Naeem: first-draft preparation, reviewing and editing, visualization, validation; Amina Sadiq: formal analysis; Hanan A. Ogaly: formal analysis and funding acquisition; Ehsan Ullah Mughal: supervision, main idea, reviewing and editing, visualization, validation, final writing the manuscript.

Conflicts of interest

Authors have no conflicts of interest to declare.

Data availability

No primary research results, software or code have been included and no new data were generated or analyzed as part of this review.

Acknowledgements

The authors extend their appreciation to the Deanship of Research and Graduate Studies at King Khalid University for funding this work through Large Research Project under grant number RGP2/95/46.

References

1 F. Bray, M. Laversanne, E. Weiderpass and I. Soerjomataram, *Cancer*, 2021, **127**, 3029–3030.
2 J. Zugazagoitia, C. Guedes, S. Ponce, I. Ferrer, S. Molina-Pinelo and L. Paz-Ares, *Clin. Ther.*, 2016, **38**, 1551–1566.
3 D. T. Debela, S. G. Muzazu, K. D. Heraro, M. T. Ndalama, B. W. Mesele, D. C. Haile, S. K. Kitui and T. Manyazewal, *SAGE Open Med.*, 2021, **9**, 20503121211034366.
4 C. A. Robertson, D. H. Evans and H. Abrahamse, *J. Photochem. Photobiol., B*, 2009, **96**, 1–8.
5 P. Agostinis, K. Berg, K. A. Cengel, T. H. Foster, A. W. Girotti, S. O. Gollnick, S. M. Hahn, M. R. Hamblin, A. Juzeniene and D. Kessel, *Ca-Cancer J. Clin.*, 2011, **61**, 250–281.
6 P.-C. Lo, M. S. Rodríguez-Morgade, R. K. Pandey, D. K. Ng, T. Torres and F. Dumoulin, *Chem. Soc. Rev.*, 2020, **49**, 1041–1056.
7 Z. Jiang, J. Shao, T. Yang, J. Wang and L. Jia, *J. Pharm. Biomed. Anal.*, 2014, **87**, 98–104.
8 W. Borzęcka, A. Domiński and M. Kowalczuk, *Nanomaterials*, 2021, **11**, 2426.
9 L. Xia, X. Kong, X. Liu, L. Tu, Y. Zhang, Y. Chang, K. Liu, D. Shen, H. Zhao and H. Zhang, *Biomaterials*, 2014, **35**, 4146–4156.
10 D. K. Chatterjee, L. S. Fong and Y. Zhang, *Adv. Drug Delivery Rev.*, 2008, **60**, 1627–1637.
11 A. M. Bugaj, *Photochem. Photobiol. Sci.*, 2011, **10**, 1097–1109.
12 M. Gupta, A. Sahu, T. Mukherjee, S. Mohanty, P. Das, N. Nayak, S. Kumari, R. P. Singh and A. Pattnaik, *Photochem. Photobiol. Sci.*, 2024, 1–24.
13 K. Plaetzer, B. Krammer, J. Berlanda, F. Berr and T. Kiesslich, *Laser Med. Sci.*, 2009, **24**, 259–268.
14 T. Dai, B. B. Fuchs, J. J. Coleman, R. A. Prates, C. Astrakas, T. G. St. Denis, M. S. Ribeiro, E. Mylonakis, M. R. Hamblin and G. P. Tegos, *Front. Microbiol.*, 2012, **3**, 120.
15 Y. Gao, Y. Li, Z. Xu, S. Yu, J. Liu and H. Sun, *Aggregate*, 2024, **5**, e420.
16 B. Dinda and B. Dinda, *Essentials of Pericyclic and Photochemical Reactions*, 2017, 181–214.
17 T. K. Horne and M. J. Cronjé, *Chem. Biol. Drug Des.*, 2017, **89**, 221–242.
18 G. Singh and S. Chandra, *Electrochem. Sci. Adv.*, 2023, **3**, e2100149.
19 K. Kadish, R. Guilard and K. M. Smith, *The Porphyrin Handbook: Phthalocyanines: Structural Characterization*, Academic Press, 2012.
20 Z. Liu, M. Li, Q. Xie, Y. Liu, J. Huang, Q. Zeng, X. Li, K. Rao, J. Ning and M. Zhao, *Nat. Commun.*, 2025, **16**, 6499.
21 S. Yang, Y. Yu, X. Gao, Z. Zhang and F. Wang, *Chem. Soc. Rev.*, 2021, **50**, 12985–13011.
22 Y. Chen, Y. Deng, Y. Li, Y. Qin, Z. Zhou, H. Yang and Y. Sun, *ACS Appl. Mater. Interfaces*, 2024, **16**, 21546–21556.
23 B.-D. Zheng, Q.-X. He, X. Li, J. Yoon and J.-D. Huang, *Coord. Chem. Rev.*, 2021, **426**, 213548.
24 M. Wang and K. Ishii, *Coord. Chem. Rev.*, 2022, **468**, 214626.
25 D. S. Jeong, H. S. Shin and J. Yang, *Sci. China Mater.*, 2022, **65**, 3324–3333.
26 O. A. Hamad, R. O. Kareem and P. K. Omer, *J. Chem. Rev.*, 2024, **6**, 39–75.
27 X. Zhang, C. Wolf, Y. Wang, H. Aubin, T. Bilgeri, P. Willke, A. J. Heinrich and T. Choi, *Nat. Chem.*, 2022, **14**, 59–65.
28 D. Mamand, T. K. Anwer, H. Qadr and C. H. Mussa, *Russ. J. Gen. Chem.*, 2022, **92**, 1827–1838.
29 R. R. Cranston and B. H. Lessard, *RSC Adv.*, 2021, **11**, 21716–21737.
30 B.-D. Zheng, J. Ye, X.-Q. Zhang, N. Zhang and M.-T. Xiao, *Coord. Chem. Rev.*, 2021, **447**, 214155.
31 R.-M. Ion, *Phthalocyanines Some Curr. Appl.*, 2017, **9**, 189–221.
32 D. Chen, M. Song, J. Huang, N. Chen, J. Xue and M. Huang, *J. Innovative Opt. Health Sci.*, 2020, **13**, 2030009.
33 K. Liu, Z. Jiang, R. A. Lalancette, X. Tang and F. Jäkle, *J. Am. Chem. Soc.*, 2022, **144**, 18908–18917.

34 M. E. Ragoussi, M. Ince and T. Torres, *Eur. J. Org Chem.*, 2013, **2013**, 6475–6489.
35 Z. Liu, L. Si, S. Shi, J. Li, J. Zhu, W. H. Lee, S.-L. Lo, X. Yan, B. Chen and F. Fu, *IEEE J. Biomed. Health Inform.*, 2024, **28**, 5270–5279.
36 A. Galstyan, *Chem.–Eur. J.*, 2021, **27**, 1903–1920.
37 X. Ma, H. Cheng, J. Hou, Z. Jia, G. Wu, X. Lü, H. Li, X. Zheng and C. Chen, *Chin. Opt. Lett.*, 2020, **18**, 051701–051712.
38 J. Li, X. Wang, C. Zhao, H. Wang, L. Lv, Z. Li and Z. Wang, *Colloids Surf., B*, 2025, **254**, 11482–11497.
39 S. Yan, J. Chen, L. Cai, P. Xu, Y. Zhang, S. Li, P. Hu, X. Chen, M. Huang and Z. Chen, *J. Mater. Chem. B*, 2018, **6**, 6080–6088.
40 L. Guo, Z. Fu, H. Li, R. Wei, J. Guo, H. Wang and J. Qi, *Adv. Colloid Interface Sci.*, 2025, 103470.
41 M.-S. Liao, T. Kar, S. M. Gorun and S. Scheiner, *Inorg. Chem.*, 2004, **43**, 7151–7161.
42 H. Yuan, Y. Chen, Y. Hu, Y. Li, H. Zhang, S. Zhang, Q. Chen, W. Zhou, J. Sun and Z. He, *J. Pharm. Invest.*, 2025, 1–14.
43 K. L. M. Santos, R. M. Barros, D. P. da Silva Lima, A. M. A. Nunes, M. R. Sato, R. Faccio, B. P. G. de Lima Damasceno and J. A. Oshiro-Junior, *Photodiagn. Photodyn. Ther.*, 2020, **32**, 102032.
44 S. Singh, A. Aggarwal, N. D. K. Bhupathiraju, G. Arianna, K. Tiwari and C. M. Drain, *Chem. Rev.*, 2015, **115**, 10261–10306.
45 D. Gounden, N. Nombona and W. E. van Zyl, *Coord. Chem. Rev.*, 2020, **420**, 213359.
46 H. Abrahamse, C. A. Kruger, S. Kadanyo and A. Mishra, *Photomed. Laser Surg.*, 2017, **35**, 581–588.
47 S. S. Lucky, K. C. Soo and Y. Zhang, *Chem. Rev.*, 2015, **115**, 1990–2042.
48 C. Feng, Y. Wang, J. Xu, Y. Zheng, W. Zhou, Y. Wang and C. Luo, *Pharmaceutics*, 2024, **16**, 1582–1598.
49 Y. Wang, Y. Xu, J. Song, X. Liu, S. Liu, N. Yang, L. Wang, Y. Liu, Y. Zhao and W. Zhou, *Int. J. Nanomed.*, 2024, 5837–5858.
50 M. Q. Mesquita, C. J. Dias, S. Gamelas, M. Fardilha, M. G. Neves and M. A. F. Faustino, *An. Acad. Bras. Cienc.*, 2018, **90**, 1101–1130.
51 J. Chen, T. Fan, Z. Xie, Q. Zeng, P. Xue, T. Zheng, Y. Chen, X. Luo and H. Zhang, *Biomaterials*, 2020, **237**, 119827.
52 S. Kwiatkowski, B. Knap, D. Przystupski, J. Saczko, E. Kędzierska, K. Knap-Czop, J. Kotlińska, O. Michel, K. Kotowski and J. Kulbacka, *Biomed. Pharmacother.*, 2018, **106**, 1098–1107.
53 M. Miretti, C. G. Prucca, T. C. Tempesti and M. T. Baumgartner, *Curr. Med. Chem.*, 2021, **28**, 5339–5367.
54 D. Diaz-Diestra, H. M. Gholipour, M. Bazian, B. Thapa and J. Beltran-Huarac, *Nanoscale Res. Lett.*, 2022, **17**, 33.
55 Y. Gao, Y. Wang, J. Jiang, P. Wei and H. Sun, *Small*, 2025, **21**, 1–11.
56 N. E.-A. El-Naggar, M. H. Hussein and A. A. El-Sawah, *Sci. Rep.*, 2017, **7**, 10844.
57 N. W. N. Simelane, G. G. Matlou and H. Abrahamse, *Int. J. Mol. Sci.*, 2023, **24**, 1902.
58 J. Van Lier, *Photodynamic Therapy Of Neoplastic Disease*, 1990, 1, 279–291.
59 L. C. Nene and T. Nyokong, *J. Photochem. Photobiol., A*, 2023, **435**, 114339.
60 D. Ma, H. Zhang, M. Zhao, A.-r. Liao, Q.-r. Peng, W.-w. Jiang and M. Yang, *J. Drug Delivery Sci. Technol.*, 2023, **87**, 104870.
61 N. W. Nkune and H. Abrahamse, *Pharmaceutics*, 2023, **15**, 2264.
62 Ö. İ. Öney, H. Y. Yenilmez, D. Bahar, N. F. Öztürk and Z. A. Bayır, *Dalton Trans.*, 2023, **52**, 13119–13128.
63 K. Aikelamu, J. Bai, Q. Zhang, J. Huang, M. Wang and C. Zhong, *Pharmaceutics*, 2024, **16**, 1166.
64 L. C. Nene, N. W. Nkune and H. Abrahamse, *J. Inorg. Biochem.*, 2024, **256**, 112570.
65 Z. Pan, Y. Li, W. Bu, W. Zhang, Y. Li, T. Meng, Z. Hu and G. Zhou, *Mater. Today Commun.*, 2024, **41**, 110914.
66 N. W. Nkune and H. Abrahamse, *RSC Adv.*, 2024, **14**, 19490–19504.
67 N. W. N. Simelane and H. Abrahamse, *Front. Mol. Biosci.*, 2024, **10**, 1340212.
68 O. C. Didamson, R. Chandran and H. Abrahamse, *Front. Oncol.*, 2024, **14**, 1338802.
69 S. Lai, B. Wang, K. Sun, F. Li, Q. Liu, X.-A. Yu, L. Jiang and L. Wang, *Molecules*, 2024, **29**, 1845.
70 Y. Tian, N. Carrillo-Malani, K. Feng, J. Miller, T. M. Busch, K. M. Sundaram, Z. Cheng, A. Amirshaghaghi and A. Tsourkas, *Nanotheranostics*, 2024, **8**, 100.
71 M. M. Simões, K. L. Paiva, I. F. de Souza, V. C. Mello, I. G. Martins da Silva, P. E. N. Souza, L. A. Muehlmann and S. N. Báo, *Pharmaceutics*, 2024, **16**, 941.
72 Y. Shen, J. Zhou, G. Chen, J. Wang, Q. Ye, K. Chen, L. Qiu, L. Chen and Y. Peng, *J. Lumin.*, 2025, **277**, 120900.
73 K. Malarz, W. Borzęcka, P. Ziola, A. Domiński, P. Rawicka, K. Bialik-Wąs, P. Kurcok, T. Torres and A. Mrozek-Wilczkiewicz, *Bioorg. Chem.*, 2025, **155**, 108127.
74 Q. Ye, F. Zheng, Z. Huang, J. Wang, G. Chen, Y. Shen, K. Chen, J. Chen, H. Sun and Y. Peng, *Sens. Actuators, B*, 2025, **433**, 137517.
75 L. Chen, L. Li, H. Zhao, H. Li, J. Li, C. Li, Y. Zhou, L. Yang, J. Liang, H. Zhang, J. Li, C. Yuan, Z. Liu, M. Huang and L. Jiang, *Colloids Surf., B*, 2025, **248**, 114493.
76 X. Chen, G. Chen, S. Dong, L. Qiu, R. Qiu, X. Han, Z. Wang, K. Wang and Y. Peng, *Spectrochim. Acta, Part A*, 2025, **325**, 125012.
77 M. He, Y. Bin, L. Huang, C. Li, Y. Ma, Y. Luo, S. Zhao and J. Liang, *Inorg. Chem. Front.*, 2025, **12**, 2468–2477.